UiT The Arctic University of Norway

Faculty of Science and Technology, Department of Physics and Technology

A comparative study of lens-less and lens-based optical imaging using full electric field analysis

Jon-Richard Sommernes

Master's thesis in physics - 60 ECTS - FYS-3900 - May 2021

"It's the questions we can't answer that teach us the most. They teach us how to think. If you give a man an answer, all he gains is a little fact. But give him a question and he'll look for his own answers."

- Patrick Rothfuss

Abstract

The focus of this thesis is to investigate the feasibility of a lens-less label-free microscope system, and compare this with a conventional lens-based microscope. The imaging performance of conventional microscopes are greatly dependent on the objective lens, due to their inherent physical space constraint and spherical aberrations. We, therefore, will investigate the conceptual feasibility of a lens-less label-free microscope, by analyzing the electromagnetic scattering directly.

Here, a lens-less design is considered. Imaging is achieved through the reconstruction of refractive index of specimens using full-electric-field analysis. The imaging performances are compared with results from lens-based microscopes. We will also briefly discuss intensity-only reconstruction, and discuss the benefits and weaknesses of such a technique.

While lens-based systems are limited by physical space limitations, the limitations of the lens-less system is similar and harder to overcome. Additionally, the lens-based system shows a non-linear proportionality with wavelengths, that the lens-less system is incapable of. The difference in setup and reconstruction results makes a preferred method dependent on the use case.

The possibility of intensity-only imaging is considered. The methods explored are phase reconstruction and a modified MUSIC algorithm.

Acknowledgements

First and foremost, I would like to thank my supervisors, Krishna Agarwal, Daniel Henry Hansen, and Zicheng Liu. Your guidance this year has been invaluable, and our interesting discussions have taught me more than I thought was possible during a year.

To my friends and office mates. You have made these two semesters more fun, and more stressful in the end, than it would otherwise be. Our idle chit chat has both wasted many hours, and given me ideas to pursue for this thesis.

To COVID-19. Thanks for making this yearlong quarantine possible. With your help, I have spend many weekends at home writing and thinking about my thesis, that I would otherwise have spend partying with my previously mentioned friends.

Contents

List of Figures

Abbreviations

DGF	Dyadic Green's Function
TR	Time Reversal
NA	Numerical Aperture
PSF	Point Spread Function
OTF	Optical Transfer Function
MUSIC	Multiple Signal Classification

Selected Symbols

The following list contains a selection of the most used constants and symbols in this thesis.

Constants

ϵ_0	Permittivity of free space	8.85×10^{-12} Fm^{-1}
μ_0	Permeability of free space	$4\pi \times 10^{-7}$ Hm^{-1}
c	Speed of light in vacuum	299 792 458 ms^{-1}

Symbols

ϵ	Permittivity of medium
μ	Permeability of medium
λ	Wavelength of light
ω	Angular frequency of light
k	Wavenumber of medium
c_n	Propagation celerity of light in medium

Notation

$\vec{A}$	Vector
$\hat{A}$	Unit vector
$\mathbf{A}$	Matrix
$A^\dagger$	Conjugate transpose
$\overline{A}$	Complex conjugate

CHAPTER 1

Introduction

Fluorescence microscopy is widely used for studying cell biology. However, undesirable traits inherent to the method can limit its usefulness. Photobleaching limits the number of photons each fluorophore will emit, thereby compromising signal to noise levels and the viable length of an experiment. Limited quantum efficiency and number of fluorophores attached to a sample in some cases requires high intensity of excitation. This excitation light will be toxic to some cells, limiting the techniques viability in live cell studies. The fluorescent dyes also makes chemical bond with the material it bonds with, changing the nature of the material. Therefore, label-free imaging is in demand. In this thesis, label-free imaging is investigated using full electric field analysis of point-like scatterers.

Further, the imaging performances of conventional optical microscopes greatly depends on the microscope objective lens. Designing and fabricating aberration-free high NA objective lenses requires relatively complex optical systems, with high quality optical elements and precise construction. This makes these components costly. Further, practical imaging systems using a single collection objective limits the collection cone to less then one hemisphere which in turn limits the achievable resolution. These inherent limitations of the lens-based system may be circumvented by directly sampling the electric fields in the sample space.

Here, the resolution of a lens-less system is simulated and compared to a conventional microscope. By analysing the full electric field for simulated systems in both cases, a good estimate of the difference in resolution may be gained. The simulations done in this thesis analyses the electric field at point-like detectors, for discrete time points.

CHAPTER 2

Forward Models

2.1 Lens Refraction

Optical microscopy is a method of magnifying an area of interest, such that something too small to be viewed with the naked eye can be seen. The imaging performance of microscopy is quantified by magnification, resolution, and contrast. In its simplest form, a modern microscope is composed of no more than two lenses as shown in Figure 2.1. In a conventional microscope, the magnification and the resolution are determined by the configurations of lenses.

The function of a lens in a microscope is to refract light. For the scatterer located at the focal point of the objective lens, the light scattered will propagate through the objective lens and tube lens and finally form the image of the the scatterer at the focal point of the tube lens. The distance from the center of the objective lens to its focus plane (focal length) is f_o. The focal length of the tube lens is f_t. For an object to be imaged in focus, thus giving us the best possible reconstruction of it, the object must be on the focal plane (one focal length away from the lens) of the objective lens, and the camera must lie in the focal plane of the tube lens. The magnification of the microscope is then given by:

$$M = \frac{f_t n_o}{f_o n_t},$$

where n_t and n_o are the refractive indexes in the object space and camera space respectively.

Due to the limited aperture of the lens, only scattered lights within the collection cone finally contribute to the reconstruction of scatterers' image.

The lost information leads to imperfect imaging. The imperfection can be quantified by the so-called point spread function (PSF). After light is refracted by the objective lens, all rays originating from the same point will travel in parallel. When being refracted by the tube lens, the parallel rays will be refocused into the PSF. In other terms, each lens in the microscope perform a Fourier transform on the light. Using this setup, all lights emitted within the solid angle the objective lens occupy (aperture) are used in the image formation.

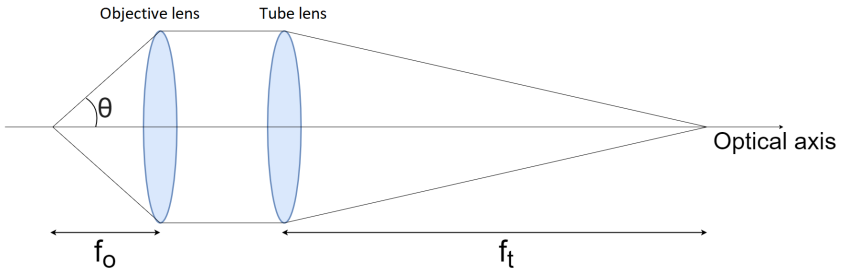

Figure 2.1: Simple microscope composed of an objective lens and a tube lens. The objective lens has a focal length (distance from lens center to lens focus) of f_o. The tube lens has a focal length of f_t. The maximum angle from the optical axis to the objective lens is θ.

2.2 Resolution limit

The aperture of the microscope determines how much of the light emitted by the sample, is used in the image reconstruction. This amount of light impacts the resolution of the microscope. This resolution limit is thus determined by the maximum angle, θ, of the cone of light that can hit the objective lens. A system where the resolution is limited by θ is called a diffraction limited system. This resolution limit can be approximated by the Abbe limit given in Equation (2.1), or the Rayleigh limit given in Equation (2.2),

$$d = \frac{\lambda}{2NA}, \tag{2.1}$$

$$d = \frac{1.22\lambda}{2NA}, \tag{2.2}$$

where d is the smallest distinguishable distance between two point scatterers in the system, and NA is the numerical aperture (NA) of the objective lens. The numerical aperture is a measure of the aperture size times the refractive index in the object space, and is given by $\mathrm{NA} = \mathrm{n} \sin\theta$.

The diffraction limit can be visualised by the optical transfer function (OTF), or the point spread function (PSF). The objective lens, and thus the pupil function, of a conventional microscope is shaped like a spherical cap. The OTF of the system can then be calculated as an autocorrelation of the pupil function[1]. The PSF of the system can then be obtained by the Fourier transform of the OTF[1].

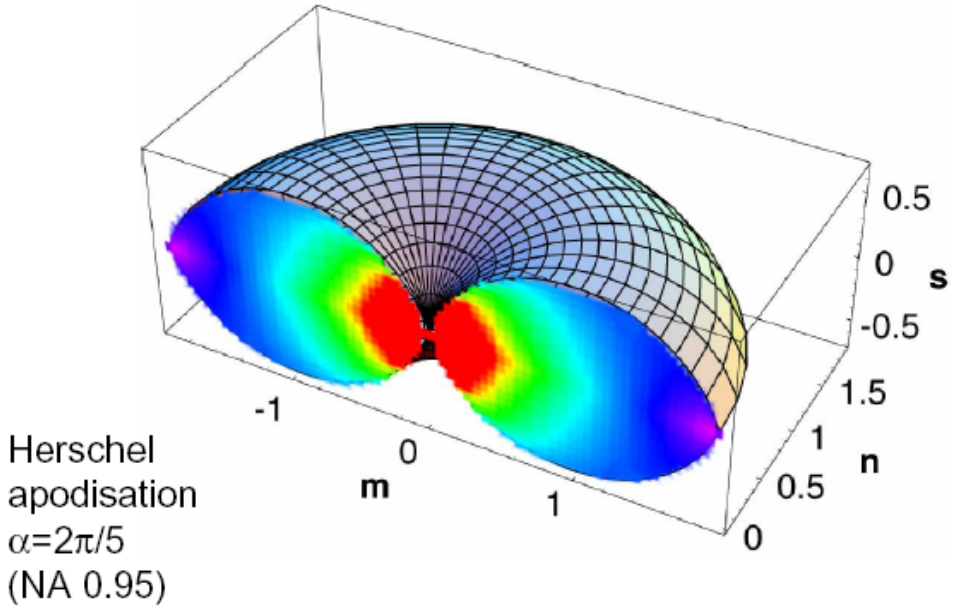

Figure 2.2: Cross section of OTF for a conventional microscope[1]. The m- and n-axis show he resolvable resolutions on the focal plane, and the s-axis show the resolvable resolutions along the optical axis.

The form of the OTF of a conventional microscope is seen in Figure 2.2. The resolvable frequencies of a microscope will be enclosed within the surface of the OTF. The OTF of a conventional microscope will be shaped like a doughnut, with a resolvable distance tending to zero along the optical axis. Along the m- and n-axis of the figure, the resolvable frequencies in the focal plane is represented. Along the s-axis the resolvable frequencies along the

optical axis is shown. The OTF, shown in Figure 2.2, clearly shows the resolution in the focal plane being much larger than along the optical axis. From the OTF we can thus find the highest resolvable frequency in any direction. The lowest resolvable distance between two point sources can then be found by d = 1/f, where d is the smallest resolvable distance, and f is the highest resolvable frequency.

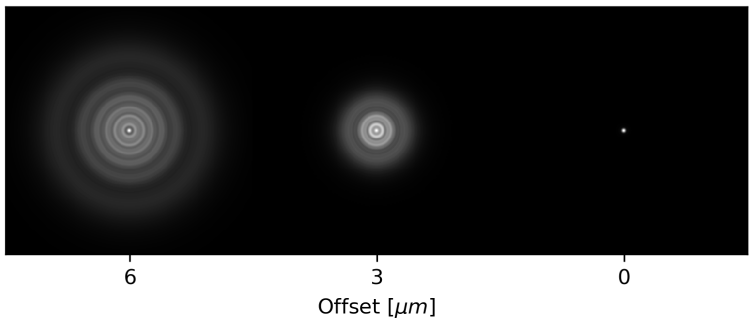

Figure 2.3: Cross section of PSF for optical axis offset of 6-, 3-, and 0 μm.

This effect can also be visualized using the PSF. This can be obtained, as mentioned earlier, by the Fourier transform of the OTF. The PSF describes how a single point is imaged by the microscope[2]. A figure showing different focal plane cross sections of a PSF is shown in Figure 2.3. The figure shows 3 cross sections, representing the PSF of a point 6-, 3-, and 0 μm away from the focus, respectively. If we assume no spherical aberrations in the system, the PSF cross section will be the same for two points with equal offset in opposite direction. Thus the PSF will be symmetric around the focal plane. Using the Airy disc (two-dimensional PSF), we can visualize

the resolution limit. Consider the Airy discs in Figure 2.4, showing the Airy discs of two points. The two Airy discs are observed at three different distances separating them. Above the Airy discs is a line profile showing the sampled intensities along the line connecting the centers of Airy discs. The total intensity of a pixel is then quantified by superposing of sampled pixels (with phase) at same locations. If the points are far enough apart, that the total intensity profile has a significant enough dip, the distance is resolvable. How significant this dip needs to be is what separates the Abbe- and Rayleigh limit.

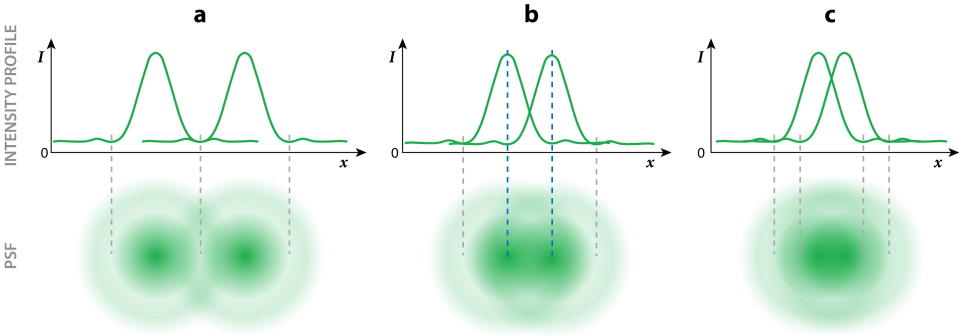

Figure 2.4: Airy discs from two point emitters (bottom), and the line profiles of each emitter (top) for the cases: **a:** Resolved emitters, **b:** Emitters resolved by the Rayleigh limit, **c:** Unresolved emitters[3]

These resolution limits can be used for conventional microscopy. If we use another imaging technique, the resolution limit must also be calculated differently. When we reconstruct an image, the main idea represented in Figure 2.4 can still be used. If we use the dip between the intensity peaks, an image will be resolvable if the intensity dip is significant enough. For this reason we use the modified Rayleigh limit. This resolution limit gives us the criterion[4]:

$$\frac{\mathrm{I}_{\mathrm{saddle}}}{\min(\mathrm{I}_{\mathrm{peaks}})} \leq 0.735, \tag{2.3}$$

where $\mathrm{I}_{\mathrm{saddle}}$ is the intensity of the saddle point between the peaks, and $\min(\mathrm{I}_{\mathrm{peaks}})$ is the minimum of the peak intensities. This criterion can then be used to estimate the resolution limit of an imaging system. Comparisons of different imaging systems can be made by studying the corresponding

resolution limits.

2.3 Fluorescence Microscopy

One way to induce contrast in a sample is by using fluorescent dyes. A fluorescent dye is a chemical that can attach to a specific element within a sample, and is capable of being excited by a photon in its excitation spectrum, then de-exciting by emitting of a photon with longer wavelength in its emission spectrum. This is called labeling a part of the sample. A sample may contain several kinds of labels working in different wave bands. This ability to selectively label specific parts of the sample is useful because it allows excluding contributions from structures in the samples that are not of interest. This may give the image good contrast, and removes factors not of interest from the image. Labels with non-overlapping emission spectra targeting different structures are available, enabling observation of several structures of interest. If there are several parts of the sample being imaged at different wave bands, the images may be combined to show the image of the sample with an improved quality.

However, when labeling of samples may give great contrast and image only parts of interest, it is not without drawbacks. Because a label must only attach to a specific part of the sample, the label makes a chemical bond with the sample. This chemical bond will alter the sample, and some characteristic of the sample may change. Different labels also require band limited light sources to excite them, as well as components in the collection path to collect only the relevant parts of the spectrum for the correspond label. this adds cost and complexity to the imaging system. This gives an additional cost to the imaging.

Fluorescent dyes also suffers from photobleaching. When exited by light, a fluorophore may alter its chemical composition and become unable to fluoresce, making the fluorophore ineffective. An excited fluorophore may also re-emit the excitation energy as heat, which may damage the sample. Another drawback of fluorophores is blinking. A fluorophore may transition into a dark state, in which the fluorophore will be unable to fluoresce for the duration. This may make a fluorophore not appear in a image of the sample.

2.4 Label-Free Microscopy

To circumvent the drawbacks of fluorescent microscopy, label-free imaging techniques are in demand. Although there are several imaging techniques for label-free imaging, the main focus of this thesis will be imaging using full electric fields using the multiple signal classification algorithm.

2.5 Imaging Systems

The image reconstruction in this thesis was done for two different imaging systems, to compare the different methods. The first system was a conventional microscope with a camera using point-like detectors. Imaging using a microscope is explained briefly in Section 2.1, and will not be repeated here.

The second imaging system to be simulated was a lens-less aperture, using point-like detectors in a spherical grid around the sample space. For the distribution of detectors, the spherical Fibonacci mapping was used. This mapping algorithm will give a near-uniform distributions of points on a sphere. Figure 2.5 shows an example of this mapping, 300 detectors distributed on a sphere with the radius of ten wavelengths. An in depth look at the algorithm can be found in Appendix C.

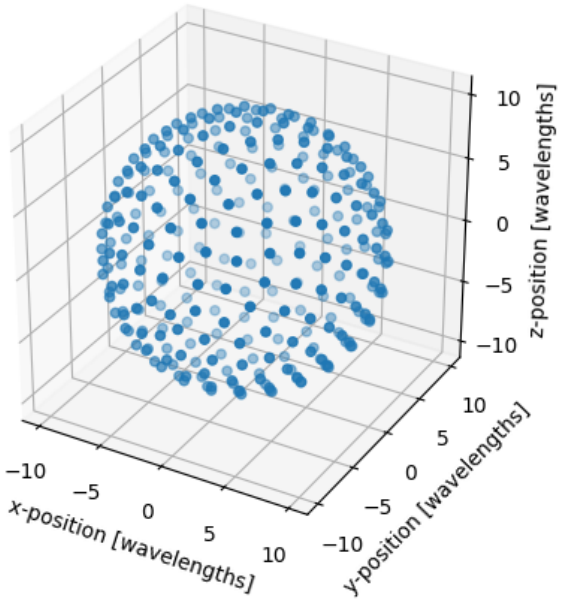

Figure 2.5: Detector location in 3D-space

2.6 Dyadic Green's Function

The dyadic Green's function (DGF) gives us a way to find the electric field from an arbitrarily orientated dipole, at any position $\vec{r}$ relative to the dipole. The DGF is a 3×3 tensor, the columns of which denote field solutions due to x-, y-, and z-polarized dipoles, respectively. For a dipole oriented along $\hat{a}$, the electric field can be found simply by a dot product of the DGF and the corresponding weights. This gives us a powerful tool for computing the electric field for a dipole at different time points, as the dipole orientation may have time variations.

2.6.1 Free space

Finding the DGF in free space is done by solving the field equation for a point source. Given the scalar wave equation this results in the equation[5]:

$$\left(\nabla^2 + \mathrm{k}^2\right) \mathrm{g}(\vec{\mathrm{r}}, \vec{\mathrm{r}}') = -\delta(\vec{\mathrm{r}} - \vec{\mathrm{r}}'), \tag{2.4}$$

where δ is the three dimensional delta function at source point $\vec{\mathrm{r}}'$, k is the wavenumber for the emitted light, ∇ is the del operator, and $\vec{\mathrm{r}}$ is the observation point. The solution to Equation (2.4) is[5]:

$$\mathrm{g}(\vec{\mathrm{r}}, \vec{\mathrm{r}}') = \frac{e^{\mathrm{i}\mathrm{k}|\vec{\mathrm{r}} - \vec{\mathrm{r}}'|}}{4\pi|\vec{\mathrm{r}} - \vec{\mathrm{r}}'|}, \tag{2.5}$$

where $|\cdot|$ is the operator measuring the length. This is the impulse response at position $\vec{\mathrm{r}}$ due to a dipole at position $\vec{\mathrm{r}}'$. Now given Maxwell's equations:

$$\nabla \times \vec{\mathrm{E}} = \mathrm{i}\omega\mu\vec{\mathrm{H}} \tag{2.6}$$

$$\nabla \times \vec{\mathrm{H}} = -\mathrm{i}\omega\epsilon\vec{\mathrm{E}} + \vec{\mathrm{J}} \tag{2.7}$$

$$\nabla \cdot \mu\vec{\mathrm{H}} = 0 \tag{2.8}$$

$$\nabla \cdot \epsilon\vec{\mathrm{E}} = \rho \tag{2.9}$$

Here ω is the angular frequency of the electromagnetic wave, $\vec{\mathrm{J}}$ is a current density, ρ is charge density, and μ and ϵ are the permeability and permittivity of the propagation medium, respectively. We can combine Equation (2.6) and Equation (2.7) and simply show that:

$$\nabla \times \nabla \times \vec{\mathrm{E}} - \mathrm{k}^2\vec{\mathrm{E}} = \mathrm{i}\omega\mu\vec{\mathrm{J}}, \tag{2.10}$$

where $\mathrm{k} = \omega\sqrt{\mu\epsilon}$. From this it can be shown that[5]:

$$\mathbf{G}\left(\vec{\mathrm{r}}, \vec{\mathrm{r}}'\right) = \left(\mathbf{I} + \frac{1}{\mathrm{k}^2}\nabla\nabla\right) \mathrm{g}\left(\vec{\mathrm{r}}, \vec{\mathrm{r}}'\right), \tag{2.11}$$

where $\mathbf{G}$ is the dyadic Green's function, $\mathbf{I}$ is the 3×3 identity matrix, g is defined in Equation (2.5), and $\mathrm{k} = \omega^2\epsilon\mu$.

If we use Equation (2.11) and express it in Cartesian coordinate system using:

$$\nabla = \frac{\partial}{\partial x}\hat{x} + \frac{\partial}{\partial y}\hat{y} + \frac{\partial}{\partial z}\hat{z} \tag{2.12}$$

The DGF can be represented in matrix form as:

$$\mathbf{G}\left(\vec{\mathrm{r}},\vec{\mathrm{r}}'\right)=\begin{pmatrix}\mathrm{k}^2+\frac{\partial^2}{\partial x^2} & \frac{\partial^2}{\partial x\partial y} & \frac{\partial^2}{\partial x\partial z}\\ \frac{\partial^2}{\partial y\partial x} & \mathrm{k}^2+\frac{\partial^2}{\partial y^2} & \frac{\partial^2}{\partial y\partial z}\\ \frac{\partial^2}{\partial z\partial x} & \frac{\partial^2}{\partial z\partial y} & \mathrm{k}^2+\frac{\partial^2}{\partial z^2}\end{pmatrix}\frac{e^{\mathrm{ik}|\vec{\mathrm{r}}-\vec{\mathrm{r}}'\ |}}{4\pi\mathrm{k}^2\left|\vec{\mathrm{r}}-\vec{\mathrm{r}}'\right|} \tag{2.13}$$

From this we see the DGF is a symmetric dyad. From the dyad we also get the vectorial information of the electrical field. Let the notation G_{ab} define the a-component of electric fields emitted by the b-oriented dipole, then the DGF can be expressed as:

$$\mathbf{G}=\begin{pmatrix}\mathrm{G}_{xx} & \mathrm{G}_{xy} & \mathrm{G}_{xz}\\ \mathrm{G}_{yx} & \mathrm{G}_{yy} & \mathrm{G}_{yz}\\ \mathrm{G}_{zx} & \mathrm{G}_{zy} & \mathrm{G}_{zz}\end{pmatrix}$$

Another way to represent the DGF is by explicitly finding the Laplacian of $\mathrm{g}\left(\vec{\mathrm{r}},\vec{\mathrm{r}}'\right)$, and using it in Equation (2.11). This will ensure a faster calculation of the field, as the implementation of this will need no calculation of derivatives. To find the Laplacian we start by finding the gradient of $\mathrm{g}\left(\vec{\mathrm{r}},\vec{\mathrm{r}}'\right)$, with the definition of $\mathrm{R}=\left|\vec{\mathrm{r}}-\vec{\mathrm{r}}'\right|$:

$$\begin{aligned}\nabla\mathrm{g}\left(\vec{\mathrm{r}},\vec{\mathrm{r}}'\right)=\nabla\mathrm{g}(\mathrm{R})&=\frac{\mathrm{d}}{\mathrm{dR}}\mathrm{g}(\mathrm{R})\nabla\mathrm{R}\\ \nabla\mathrm{g}(\mathrm{R})&=\left(\mathrm{ik}-\frac{1}{\mathrm{R}}\right)\mathrm{g}(\mathrm{R})\nabla\mathrm{R}\end{aligned} \tag{2.14}$$

The gradient of an absolute valued function can be proven to be the sign function of the non-absolute valued function. Thus we get:

$$\nabla\mathrm{R}=\frac{\vec{\mathrm{r}}-\vec{\mathrm{r}}'}{\left|\vec{\mathrm{r}}-\vec{\mathrm{r}}'\right|}=\hat{\mathrm{R}} \tag{2.15}$$

We substitute $\hat{R}$ into Equation (2.14) to get:

$$\nabla\mathrm{g}(\mathrm{R})=\left(\mathrm{ik}-\frac{1}{\mathrm{R}}\right)\mathrm{g}(\mathrm{R})\hat{\mathrm{R}} \tag{2.16}$$

We then find the gradient of this function to get the Laplacian:

$$\nabla\nabla \mathrm{g(R)} = \nabla\left[\left(\mathrm{ik} - \frac{1}{R}\right)\mathrm{g(R)}\hat{\mathrm{R}}\right]$$
$$\nabla^2 \mathrm{g(R)} = \nabla\left[\left(\mathrm{ik} - \frac{1}{\mathrm{R}}\right)\mathrm{g(R)}\right]\hat{\mathrm{R}} + \left(\mathrm{ik} - \frac{1}{\mathrm{R}}\right)\mathrm{g(R)}\nabla\hat{\mathrm{R}}$$
$$\nabla^2 \mathrm{g(R)} = \nabla\frac{1}{\mathrm{R}}\mathrm{g(R)}\hat{\mathrm{R}} + \left(\mathrm{ik} - \frac{1}{\mathrm{R}}\right)\nabla\mathrm{g(R)}\hat{R} + \left(\mathrm{ik} - \frac{1}{\mathrm{R}}\right)\mathrm{g(R)}\nabla\hat{\mathrm{R}} \quad (2.17)$$

It can be shown that:

$$\nabla\frac{1}{\mathrm{R}} = \frac{\hat{\mathrm{R}}}{\mathrm{R}^2} \quad (2.18)$$

Given $\nabla\vec{\mathrm{R}} = \mathbf{I}$, $\nabla\hat{R}$ is calculated as:

$$\nabla\hat{\mathrm{R}} = \nabla\left(\frac{\vec{\mathrm{R}}}{\mathrm{R}}\right) = \frac{\nabla(\vec{\mathrm{R}})}{\mathrm{R}} + \vec{\mathrm{R}}\nabla\left(\frac{1}{\mathrm{R}}\right)$$
$$\nabla\hat{\mathrm{R}} = \frac{\mathbf{I}}{\mathrm{R}} + \frac{\hat{\mathrm{R}}\hat{\mathrm{R}}}{\mathrm{R}} = \left(\mathbf{I} - \hat{\mathrm{R}}\hat{\mathrm{R}}\right)\frac{1}{\mathrm{R}} \quad (2.19)$$

This is inserted into Equation (2.17) to give:

$$\nabla^2 \mathrm{g(R)} = \nabla\frac{1}{\mathrm{R}}\mathrm{g(R)}\hat{\mathrm{R}} + \left(ik - \frac{1}{\mathrm{R}}\right)\nabla\mathrm{g(R)}\hat{\mathrm{R}} + \left(\mathrm{ik} - \frac{1}{\mathrm{R}}\right)\mathrm{g(R)}\nabla\hat{\mathrm{R}}$$
$$\nabla^2 \mathrm{g(R)} = \frac{\hat{\mathrm{R}}}{\mathrm{R}^2}\mathrm{g(R)}\hat{\mathrm{R}} + \left(\mathrm{ik} - \frac{1}{\mathrm{R}}\right)^2\mathrm{g(R)}\hat{\mathrm{R}}\hat{\mathrm{R}} + \left(\mathrm{ik} - \frac{1}{R}\right)\mathrm{g(R)}\left(\mathbf{I} - \hat{\mathrm{R}}\hat{\mathrm{R}}\right)\frac{1}{\mathrm{R}}$$
$$\nabla^2 \mathrm{g}(R) = \left[\left(\frac{3}{R^2} - \frac{3\mathrm{ik}}{\mathrm{R}} - \mathrm{k}^2\right)\hat{R}\hat{\mathrm{R}} + \left(\frac{\mathrm{ik}}{\mathrm{R}} - \frac{1}{\mathrm{R}^2}\right)\mathbf{I}\right]\mathrm{g(R)} \quad (2.20)$$

Equation (2.4) and Equation (2.20) is then combined to give:

$$\mathbf{G}\left(\vec{\mathrm{r}}, \vec{\mathrm{r}}'\right) = \left(\mathbf{I} + \frac{1}{\mathrm{k}^2}\nabla\nabla\right)\mathrm{g}\left(\vec{\mathrm{r}}, \vec{\mathrm{r}}'\right)$$
$$\mathbf{G}\left(\vec{\mathrm{r}}, \vec{\mathrm{r}}'\right) = \mathbf{I}\mathrm{g(R)} + \frac{1}{\mathrm{k}^2}\nabla^2\mathrm{g(R)}$$
$$\mathbf{G}\left(\vec{\mathrm{r}}, \vec{\mathrm{r}}'\right) = \mathbf{I}\mathrm{g(R)} + \left[\left(\frac{3}{\mathrm{k}^2\mathrm{R}^2} - \frac{3\mathrm{i}}{\mathrm{kR}} - 1\right)\hat{\mathrm{R}}\hat{\mathrm{R}} + \left(\frac{\mathrm{i}}{\mathrm{kR}} - \frac{1}{\mathrm{k}^2\mathrm{R}^2}\right)\mathbf{I}\right]\mathrm{g(R)}$$
$$\mathbf{G}\left(\vec{\mathrm{r}}, \vec{\mathrm{r}}'\right) = \left[\left(\frac{3}{\mathrm{k}^2\mathrm{R}^2} - \frac{3\mathrm{i}}{\mathrm{kR}} - 1\right)\hat{\mathrm{R}}\hat{\mathrm{R}} + \left(1 + \frac{i}{\mathrm{kR}} - \frac{1}{\mathrm{k}^2\mathrm{R}^2}\right)\mathbf{I}\right]\mathrm{g(R)} \quad (2.21)$$

Using Equation (2.21) the dyadic Green's function can be found for any observation position $\vec{r}$ relative to a dipole. The polarization of the dipole can then be used to find the electric field at point $\vec{r}$. The dipole polarization can be represented by:

$$\vec{P} = \begin{bmatrix} \sin(\theta)\cos(\phi) \\ \sin(\theta)\sin(\phi) \\ \cos(\theta) \end{bmatrix}, \tag{2.22}$$

where θ and ϕ are the polar and azimuthal angle of the dipole respectively. The electric field can then be calculated as:

$$\vec{E} = \mathbf{G}\vec{P} \tag{2.23}$$

The DGF for a dipole gives a 3×3 matrix output, containing electric field solution for a single observation point. For finding the DGF at multiple locations at once, the distance vector, $\vec{r}$, may be substituted by a distance matrix, $\mathbf{r}$. The new distance matrix contains the Cartesian coordinates of N different observation points. Using this as an input, and calculating the DGF for each distance vector in the matrix, the output will have the shape N×3 × 3. This output will contain the DGF for all N observation points. This makes it possible to calculate the DGF for an entire detector array simultaneously. This has the added benefit of a significantly faster calculation time.

When the DGF is found, it can be used to find the electric field for any dipole orientation. For a series of images, a dipole orientation matrix, $\mathbf{P}$, can be calculated, where the columns of $\mathbf{P}$ contain the dipole orientation at different time-points. For a series of M images, this matrix will then have the shape 3×M. This can then be replaced with the dipole vector in Equation (2.23), which will give us an output shape of 3×M for a single DGF. Doing this for all detectors in the DGF, we find an electric field tensor. This will give us a tensor of the shape N×3×M, and will contain the electric field at all detectors at all time points.

For the scope of this thesis, the dipoles are assumed to be able to re-orient itself along all axis. The orientation of a dipole at any time point can then be implemented using a random number generator. The angles of the dipole are randomized, and the orientation in Cartesian coordinates are found.

We now have a tensor containing the electric fields. To make the reconstruction algorithms simpler, the tensor is reshaped into an array. Assuming

we can use different light polarizations as independent data points, the tensor is reshaped into a matrix with dimension 3N×M. In this configuration of the DGF, the x-, y-, and z-polarized fields are contained consecutively in the array. The x-polarized field is contained in the first N rows of the matrix, the y-polarized field is contained in the next N rows, and the z-polarized field in the last N rows.

2.6.2 Microscope

When the electric field, computed based on the DGF, passes through a microscope, the lens refraction given in Section 2.1 must be considered. Light traveling from the same source will be refocused to a PSF in the camera space. Any electric field measured from a camera array will thus be a superposition of the entire field hitting the objective lens. The calculation of the DGF for a microscope is outside the scope of this thesis. The derivation of the microscope DGF can be found in [4, 6]. I will here explain my understanding of the microscope DGF. In these calculations, we assume the camera sensors are point like detectors.

Assuming an arbitrarily positioned dipole inside the field of view (FoV) in the object space. If the dipole emits light, waves will travel to and be refracted by the objective lens. How the light is refracted, and the effects of the lenses is described in Section 2.1. Further assuming the focal length of the objective lens is much larger than the emitted wavelength, the near field will be negligible and we can consider only the far field. After tracing the fields through the microscope, the superposition can be calculated by integrating over the objective lens aperture. After integrating over the aperture, we are left with a PSF containing information of the DGF gathered from the entire aperture. The electric field can then be calculated using the DGF and the dipole polarization, with Equation (2.23).

When the DGF is calculated, we find the E-field for all time points using the same method as described in Section 2.6.1. This is done for all detectors in the camera array, and the results are reshaped into a 3N×M array the same way as for the free space DGF.

CHAPTER 3

Imaging Algorithms

3.1 Time reversal

In the domain of lossless media, the electromagnetic wave equation is time symmetric[7]. This gives us the framework to built a reconstruction algorithm for electromagnetic sources. In practice, assuming we have a signal, s(r,t), emitting in the time window t$\in [0, T]$, the time reversal (TR) of s can be applied as[7]:

$$\mathrm{s(x,t)} \mapsto \mathrm{s(x, T - t)} \tag{3.1}$$

This property can be derived from the wave equation for a uniform and lossless medium. This equation can be derived from Maxwell's equations:

$$\frac{1}{\mathrm{c_n^2}} \frac{\partial^2 \mathrm{E}}{\partial \mathrm{t}^2} = \nabla^2 \mathrm{E}, \tag{3.2}$$

where E is the electric field, and $\mathrm{c_n}$ is the speed of light in the medium of refractive index n. By the symmetric nature of this differential equation, if $\mathrm{E}(\vec{\mathrm{r}}, \mathrm{t})$ is a solution, then $\mathrm{E}(\vec{\mathrm{r}}, -\mathrm{t})$ must also be a solution. Therefore the wave equation is invariant under the TR operator. This gives us the possibility to reverse a measured signal, and let it propagate back to its source.

This principle is widely used in numerous fields, such as: electromagnetism[8], submarine telecommunications [9], biomedical imaging[10], gas leak detection[11], and physical layer security in information transmission[12].

3.1.1 Detector Field and Phase Conjugate Time Reversal

Suppose V $\subset \mathbb{R}^3$ (V is a volume in three-dimensional space), bounded by the surface S= ∂V. The volume V in this case will be a sphere of radius r. Another volume W $\subset$ V is a sphere concentric with V, with a radius $\rho <$ r. A set of dipoles are present at some arbitrary points inside the volume W. The dipoles have arbitrary orientations in the 3D space.

On the surface S is an array of photo-detectors, with size N. The electrical field at detector i is represented as E_i. Using Equation (2.21), the location of each dipole, and the radius of V, we can find the DGF at each detector. We can then find the electrical field at each detector by:

$$\mathrm{E_i} = \sum_{\mathrm{j=1}}^{\mathrm{N_d}} \mathbf{G_i}\vec{\mathrm{v}}_\mathrm{j}, \tag{3.3}$$

where $\vec{\mathrm{v}}_\mathrm{j}$ indicates the orientation of the j-th dipole, and $\mathrm{N_d}$ is the number of dipoles.

Based on the electric field at all detectors, calculated by Equation (3.3), the field can be reversed at each detector using the TR operator. A simple way of implementing the time reversal operation is by taking the complex conjugate of the Fourier transformed electrical field[13], such as:

$$\mathrm{TR}\left\{\mathrm{E(r,t)}\right\} = \mathrm{E(r,-t)} = \mathcal{F}_{\mathrm{inv}}\left\{\widetilde{\mathrm{E}}^{\dagger}(\mathrm{r},\omega)\right\}, \tag{3.4}$$

where $\widetilde{\mathrm{E}}$ is the Fourier transformed electrical field, ω is the angular frequency of electrical fields, $\mathcal{F}_{inv}$ denotes the inverse Fourier transform, and † denotes the complex conjugate.

Using the time reversed signal, the detectors can be simulated as point sources emitting back into the sphere V. The field emitted by the detectors will then be focused back to the locations of the dipoles. The volume W containing the dipoles can be imaged using the time reversed field, and an image of the volume can be reconstructed.

3.2 MUSIC

The use of eigen-decomposition unlocks a set of more complex reconstruction algorithms. One such algorithm type is multiple signal classification (MUSIC). MUSIC is used to determine the parameters of multiple wavefronts arriving at an antenna array[14]. The algorithm implemented in this

paper uses the Dyadic Green's function, as described in section 2.6, and the covariance matrix of the signal array to estimate emitter position.

3.2.1 Theory and Implementation

Assuming we have a volume V $\subset \mathbb{R}^3$ containing a sample. We then have a surface S, with no overlap with volume V. On the surface S is a sensor grid imaging the full electric field from the samples.

At each sensor location a signal $\vec{E}$ is collected. Using the DGF in section 2.6, we find the electric field to be:

$$\mathbf{E} = \mathbf{GP}, \tag{3.5}$$

where $\mathbf{E}$ is the electric field, $\mathbf{G}$ is the dyadic Green's function, and $\mathbf{P}$ is the dipole polarization for differed time points. This electric field matrix will contain the full electric field for all polarizations, at all N detectors, and for M different time points. Assuming noise and signal is uncorrelated, we can find a signal matrix by:

$$\mathbf{X} = \mathbf{GP} + \mathbf{W}, \tag{3.6}$$

where $\mathbf{X}$ is the signal matrix, and $\mathbf{W}$ is additive noise. The $\mathbf{G}$ matrix will have the shape 3N×3, where Greens function in the first N rows contain the x-polarized field, the next N rows contain the y-polarized field, and the last N rows contain the z-polarized field. The $\mathbf{P}$ matrix will then be of shape 3×M, with column m containing the polarization at time point m. This representation of the data matrix shows a clear linear dependence on $\mathbf{G}$. If there are several dipoles inside the volume V, the data matrix can be calculated as:

$$\mathbf{X} = \sum_{\mathrm{k}=1}^{\mathrm{K}} \mathbf{G}_{\mathrm{k}}\mathbf{P}_{\mathrm{k}} + \mathbf{W},$$

where K is he number of dipoles. Now we can calculate the covariance matrix of $\mathbf{X}$. This will give us the joint variability between each pair of detectors over all time points. Assuming signal and noise are uncorrelated, the covariance matrix $\mathbf{S}$ is:

$$\mathbf{S} = \mathbf{X}\mathbf{X}^\dagger = \mathbf{G}\mathbf{P}\mathbf{P}^\dagger\mathbf{G}^\dagger + \mathbf{W}\mathbf{W}^\dagger \tag{3.7}$$

Since the covariance matrix is simply a matrix product, giving a sum of all time points, the inherent spatial geometry of the $\mathbf{X}$ matrix is conserved.

The number of sources, and the corresponding signal can be found using an eigenvalue decomposition of the covariance matrix. If the number of detectors is greater than the number of dipoles, the rank of $\mathbf{S}$ will be less than 3N. The rank of $\mathbf{S}$ can be determined by the number of non-zero eigenvalues of $\mathbf{S}$. The eigenvectors corresponding to non-zero eigenvalues will then represent the signal from our dipoles. The other eigenvectors will correspond to noise. In practice, no eigenvalue will be zero, but close to zero compared to eigenvalues corresponding to signal.

The noise eigenvectors can then be separated from the signal eigenvectors, to compose a noise matrix $\mathbf{E}_{\mathrm{N}}$. Because the spatial geometry of $\mathbf{X}$ is conserved in $\mathbf{S}$, the eigenvectors corresponding to non-zero eigenvalues will contain the signal from $\mathbf{X}$, and thus contain the information from $\mathbf{G}$. Because of the orthogonal structure of the eigen decomposition, the noise space spanned by $\mathbf{E}_{\mathrm{N}}$ will be orthogonal to the signal space, and thus be orthogonal to $\mathbf{G}$.

Because the eigen decomposition spans the entire space supported by the detectors, and $\mathbf{E}_{\mathrm{N}}$ is orthogonal to $\mathbf{G}$, $\mathbf{E}_{\mathrm{N}}$ will be parallel to all other signals. This gives us the means to reconstruct the dipole locations.

Now assume we calculate the DGF, $\mathbf{A}$, at the detector grid, assuming a dipole is located at an arbitrary point, $\vec{\mathrm{r}}$, in volume V. We can then test whether $\mathbf{A}$ is a component of $\mathbf{G}$, using the equation[14]:

$$\mathrm{P} = \frac{1}{\mathbf{A}^{*}\mathbf{E}_{\mathrm{N}}\mathbf{E}_{\mathrm{N}}^{*}\mathbf{A}}, \tag{3.8}$$

where P is the reconstruction estimator. If $\mathbf{A} \in \mathbf{G}$, $\mathbf{A}$ will be orthogonal to $\mathbf{E}_{\mathrm{N}}$, and the value of P will tend to infinity. Otherwise, if $\mathbf{A} \notin \mathbf{G}$, $\mathbf{A}$ will be parallel to $\mathbf{E}_{\mathrm{N}}$, and P will tend to 0.

3.3 Resolution Limit Calculation

As previously mentioned, the resolution limit of a diffraction limited system is often measured by the Abbe limit given by Equation (2.1), or the Rayleigh limit given by Equation (2.2). Henceforth we will use the Rayleigh criterion to set the resolution limit of a diffraction limited system. Similarly, we will use the modified Rayleigh limit, calculated using Equation (2.3), to measure the resolution limit of non-conventional systems.

Finding the resolution limit of a system can be done several ways. In this thesis we will use an iterative method to approach the resolution limit. A

brief explanation of the method will follow. For a detailed implementation of this method, see Appendix C.

Assuming we have a set of two dipoles at distance, d, apart. If the dipoles are resolved as two distinct points, we can reduce the distance between the points until they are no longer resolvable. When the step size is small enough relative to the distance, the resolution limit is well estimated.

In Figure 3.1 the saddle-to-peak ratio as a function of d is shown. This example uses time reversal, where the only variable is the distance between dipoles. Because the saddle-to-peak is dependent on the distance, the iterative method will work.

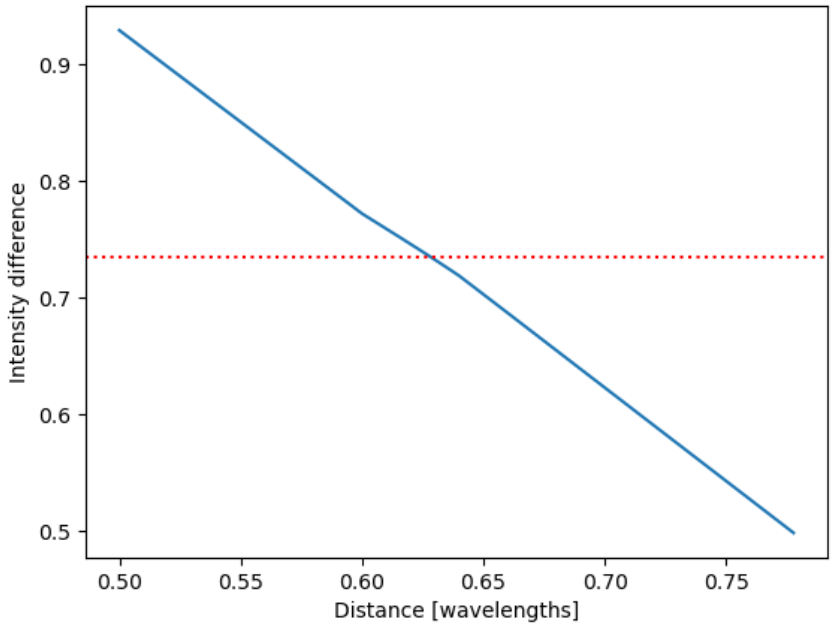

Figure 3.1: Figure showing the saddle-to-peak ratio as function of distance between dipoles (blue line), and the modified Rayleigh limit (red dotted line). The distance where the lines intersect will then be the resolution limit of the system.

Now we will look at how this method works for the MUSIC algorithm. To do this two sets of dipoles are reconstructed using MUSIC. The first set

of dipoles, found in Figure 3.2, have a saddle-to-peak ratio clearly above 0.735. This makes the two dipoles resolvable by the system. The next set of dipoles, found in Figure 3.3, have a slightly shorter distance between them. As we see in the figure, the reconstructed image shows a elongated sample. As the first sample is resolvable, but the second one is not, the resolution limit must be somewhere between the two distances. The algorithm then stops when it has found a resolvable sample, and a non-resolvable sample, that are relatively close.

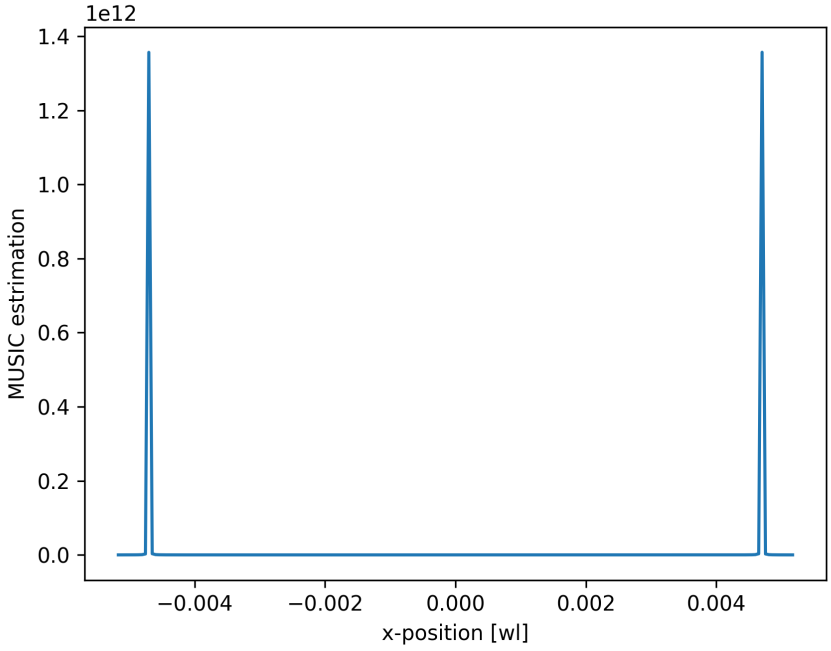

Figure 3.2: Figure showing the MUSIC reconstruction in a line intersecting two dipoles. The dipole location are found using the intensity peaks.

3.3.1 Preventing variation of the polarization matrix

For any result of the MUSIC algorithm, there is a set number of time point that are used to make the covariance matrix. Thus, if the polarization matrix changes, the results of the reconstruction might change. This use of randomness is not used in any other variable, and are thus only applicable

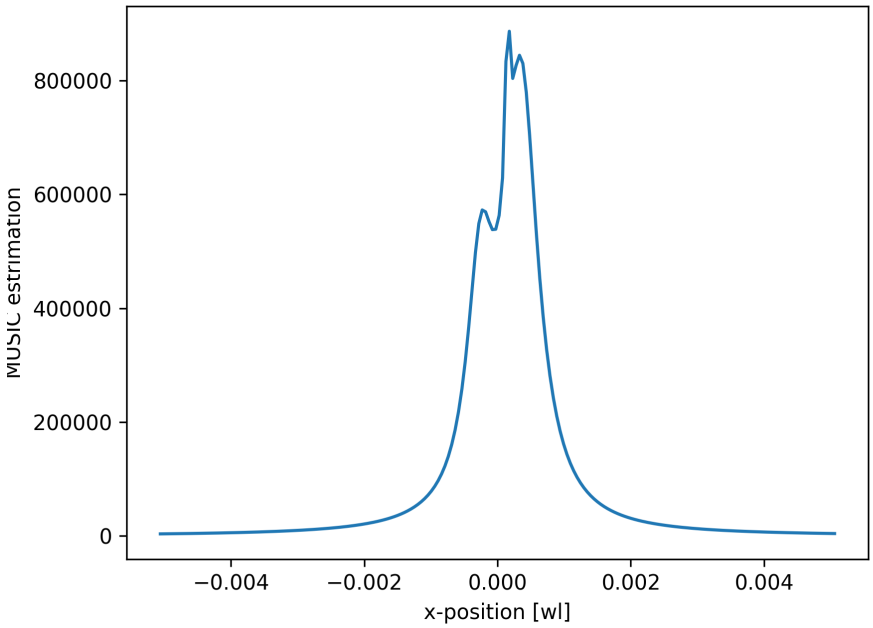

Figure 3.3: Figure showing the MUSIC reconstruction for a line intersecting two unresolved dipoles. The dipoles are to close to be reconstructed as separate points, and are instead reconstructed as an elongated sample.

for the polarization matrix. To negate this effect, a permanent polarization matrix was made. The matrix was implemented with time points, M, enough to be used for all reconstructions. When a matrix of size m<M was used, the first m elements of the polarization matrix was used. This will remove the inherent variability the polarization matrix induces.

CHAPTER 4

Results and Discussion

4.1 Time Reversal

Time reversal gives a simple and intuitive way to reconstruct an image using electric fields. For this reason, we will in this section give a view of imaging performances of time reversal technique. Comparisons to the more complex, and computational demanding MUSIC algorithm will be made. As MUSIC is the main focus of this thesis, we will briefly look at some results using time reversal.

The results in Figure 4.1 and Figure 4.2 show the resolution limit for parallel and orthogonal oriented dipoles respectively. The resolution limit is studied with various numbers of detectors. The detectors was uniformly distributed on a sphere around the dipoles. The dipoles are located at positions close to the center of the sphere. The detector grid has a radius of 10 wavelengths, where evanescent fields can be discarded.

From the results, we see a superiority in resolution for orthogonally oriented dipoles over parallelly oriented dipoles.

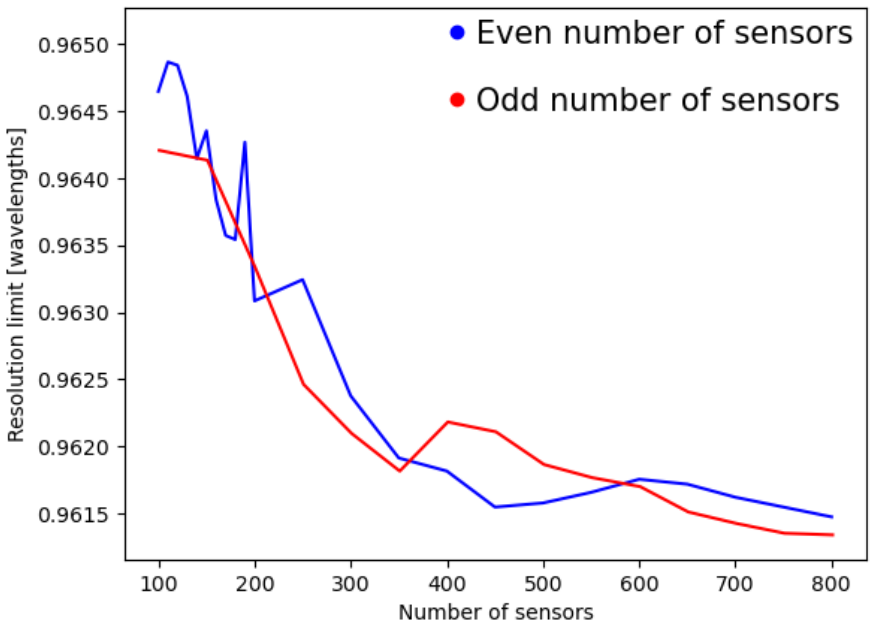

Figure 4.1: Resolution of time reversal method as a function of the sensor amount for parallel dipoles centered around origin.

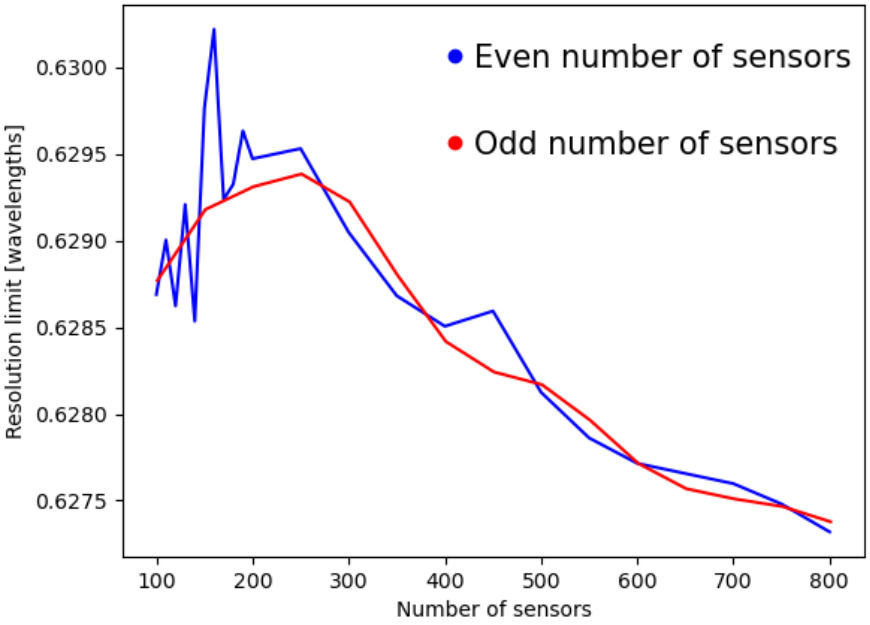

Figure 4.2: Resolution of time reversal method as a function of the sensor amount for orthogonal dipoles centered around origin.

4.2 MUSIC

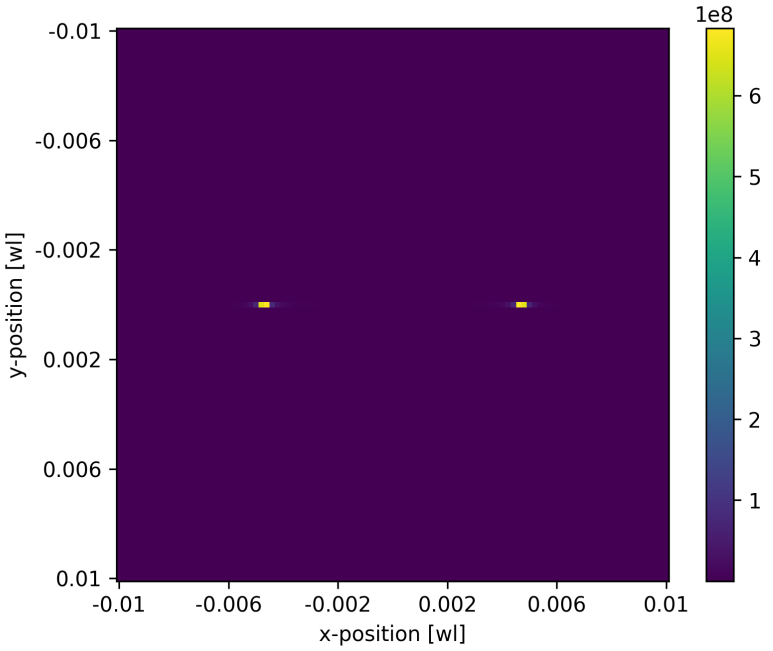

Figure 4.3: MUSIC reconstruction of a plane containing two dipoles for noise-free data. The dipoles are separated by 6.486 nm, and are concentric with the detector array. The imaged wavelength was 690 nm, and the detector array has a radius of 0.05 m.

In this section we will look at some MUSIC reconstructions, and comparing the resolution limit of a lens-less system and a microscope. In addition to comparing the two systems, we will investigate the effect of some main variables in MUSIC, such as the sensor amount, the radius of the apertures, the wavelength of scattered light, and the number of time points.

4.2.1 Lens-Less system

For the lens-less system, we have two possibilities. For a direct comparison with a microscope, we can put detectors in a spherical cap. This will sample the same space as the objective lens of the microscope. The other possibility

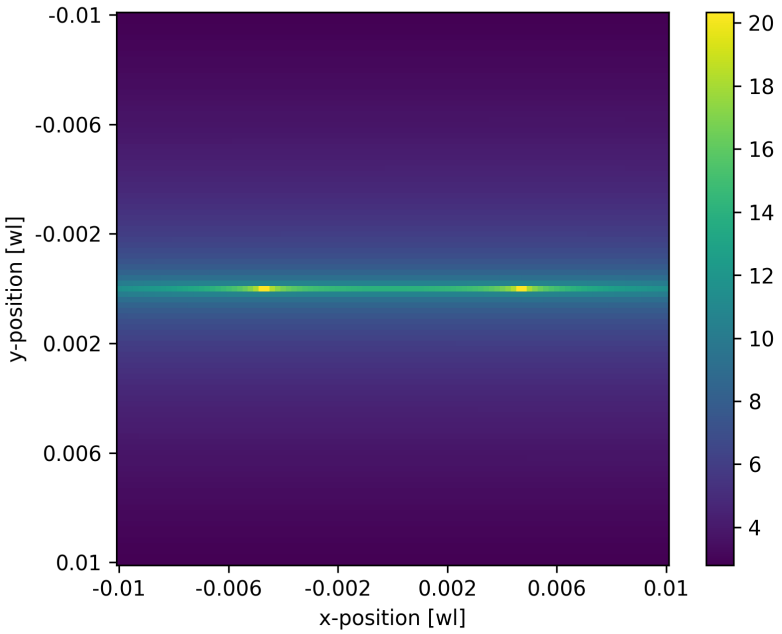

Figure 4.4: Log scale of MUSIC reconstruction of a plane containing two dipoles for noise-free data. The dipoles are separated by 6.486 nm, and are concentric with the detector array. The imaged wavelength was 690 nm, and the detector array has a radius of 0.05 m.

is using a spherical detector array. This will sample the electric field in a complete sphere. Henceforth the spherical cap will be called a semi aperture, and the full sphere is a full sphere aperture. The semi aperture may then be shaped using numerical aperture as a measure of the solid angle.

To visualize the reconstruction of the MUSIC algorithm, a 2D reconstruction of a sample space is shown in Figure 4.3. The reconstruction was done for a set of dipoles separated by 0.0094 wavelengths for a full sphere aperture. The wavelength was set to 690 nm, the number of detectors and time points was set to 100, the radius of the detector array was 5 cm, and the dipoles was centered at the array center. The values given here will be the standard values when exploring the resolution limits. For this sample, the distance between the dipoles are close to the least resolvable distance.

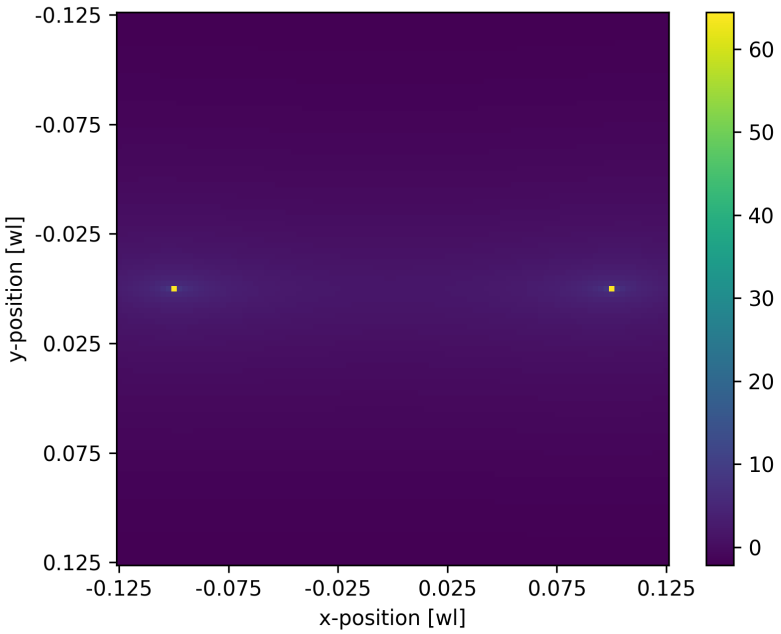

Figure 4.5: Log scale of MUSIC reconstruction of a plane containing two dipoles for noise-free data. The dipoles are separated by 138 nm, and are concentric with the detector array. The imaged wavelength was 690 nm, and the detector array has a radius of 0.05 m.

For Figure 4.3, contrast of the reconstruction is very high. To get a better look at the values between the dipoles, the natural logarithm of the image can be found in Figure 4.4. Looking at the logarithmic image, a higher reconstruction estimate can be seen in the line spanning the two dipoles. This higher reconstruction value shows a greater correlation between the DGF points along the line, than for points in other parts of the background. This line in the reconstruction is most likely a result of the near-resolution-limit distance between the dipoles. To test this, another reconstruction is given in Figure 4.5. In this reconstruction the dipoles are separated by a distance of 0.2 wavelengths. The line is still present in the reconstruction, but far less prominent than the dipoles close to the resolution limit.

Taking the same system, the distance between the dipoles is reduced to

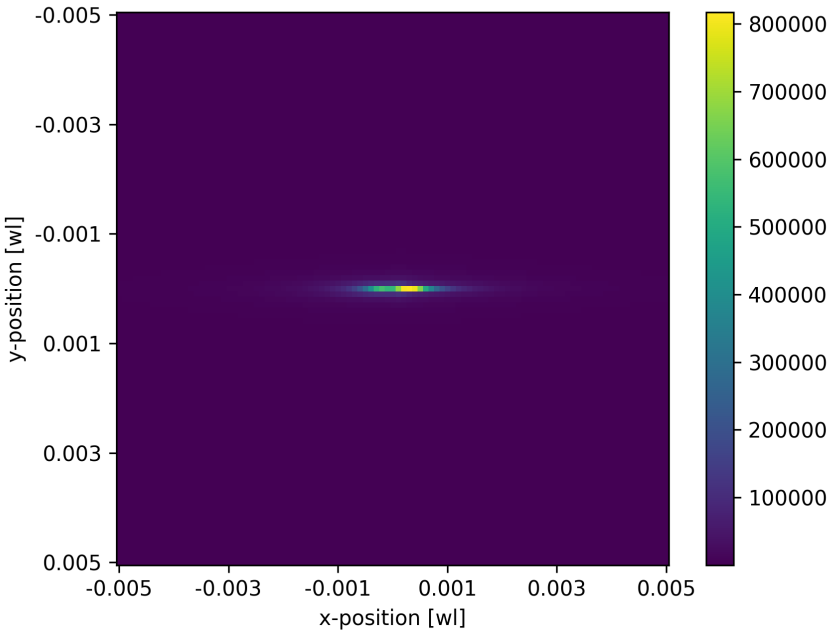

Figure 4.6: MUSIC reconstruction of a plane containing two dipoles for noise-free data. The dipoles are separated by 6.348 nm, and are concentric with the detector array. The imaged wavelength was 690 nm, and the detector array has a radius of 0.05 m

right beneath the resolution limit. The reconstruction for this case is seen in Figure 4.6. Here the reconstruction fails, and the dipoles is reconstructed as one elongated sample. The position of the sample is also in the center of the two scattering dipoles.

These reconstructions give us a good understanding of how the reconstruction behaves around the resolution limit. When two dipoles are separated by a distance much larger than the resolution limit, the dipoles are reconstructed with great accuracy. This also holds true when the distance moves towards the resolution limit, but in this case the area between the dipoles will be reconstructed with a much higher intensity than the background. Although, this increase in intensity between the dipoles will not affect the results, as the contrast is still very high. The reconstruction

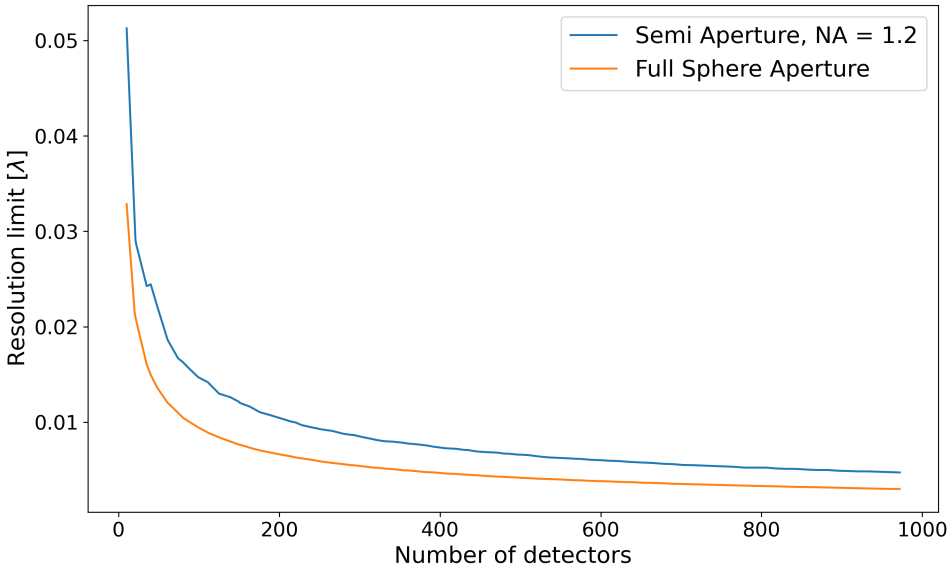

Figure 4.7: Resolution limit in wavelengths with respect to number of detectors in the imaging array using MUSIC. The blue line represents a detector array in a spherical cap, covering an area corresponding to a numerical aperture = 1.2. The orange line represents a full spherical detector array.

only breaks down when the distance is shorter than the resolution limit. In this case the dipoles are reconstructed as one elongated sample. Because the dipoles are resolvable for any distance, until the reconstruction breaks down, the resolution limit for this MUSIC implementation will be more rigid than the modified Rayleigh criterion.

Next we investigate different imaging variables, to find their effects on the resolution limit. In the following simulations we will measure the resolution limit with respect to a single variable, and all other variables will remain constant. This holds true for a single simulation, and between simulations. E.g. inn all simulations, except when finding the effect of the number of detectors, the amount of detectors will remain constant. In the case of the polarization matrix, all values are held constant as mentioned in section 3.3.1. For all simulations, the refractive index of immersion medium is held constant as 1.33. For the standard configuration of the imaging system, the number of detectors where held constant at 100, the number of time points where held at 100, the radius of the detector array was set to

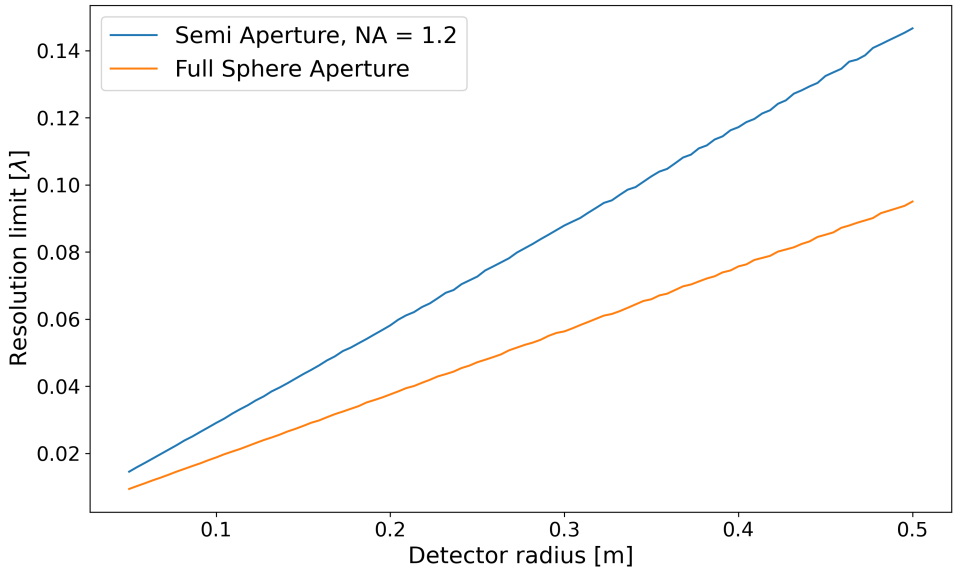

Figure 4.8: Resolution limit in wavelengths with respect to image array radius using MUSIC. The blue line represents a detector array in a spherical cap, covering an area corresponding to a numerical aperture = 1.2. The orange line represents a full spherical detector array.

be 0.05 meters, the center of the dipoles was at the center of the imaging array, the wavelength equals 690 nm, and the area containing detectors were either a full sphere aperture or equivalent to a numerical aperture of 1.2.

Looking at Figure 4.7 the resolution limit is measured with respect to the number of detectors. The blue line represents an imaging array set on a spherical cap equivalent to a 1.2 NA lens. The orange line represents a full sphere aperture. The resolution axis is given in wavelengths (690 nm). Looking at the figure, the estimated resolution limits are inverse proportional to the number of detectors. The full sphere aperture has a consistently lower resolution limit than the semi aperture.

Figure 4.8 shows the resolution limit with respect to the radius of the imaging array. The full sphere aperture (orange line) is again consistently lower than for the semi aperture (blue line). From the graphs, the resolution limit is proportional to the detector radius.

In Figure 4.9 the resolution limit is plotted with respect to the number of time points. From the figure, the resolution limit looks to be inverse

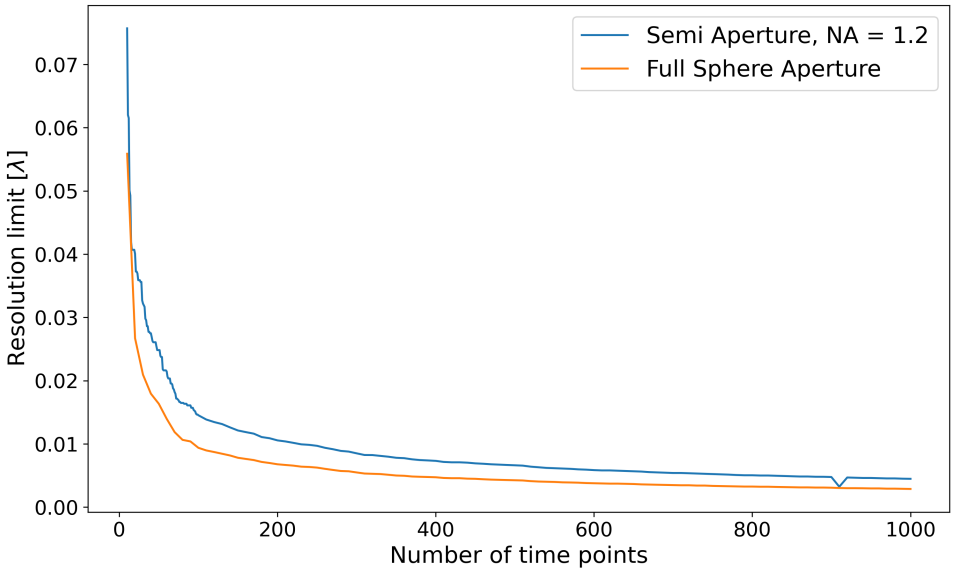

Figure 4.9: Resolution limit in wavelengths with respect to number of time points using MUSIC. The blue line represents a detector array in a spherical cap, covering an area corresponding to a numerical aperture = 1.2. The orange line represents a full spherical detector array.

proportional to the number of time points. The resolution for the full sphere aperture is consistently lower than for the semi aperture, with the exception of one point around 900 time points. This dip in resolution limit for one time point might be the result of the corresponding polarization matrix gives a better reconstruction. The single dip might also be due to a numerical error for the reconstruction. The rest of the graph, consisting of 180 samples, shows the smooth line of an inverse proportional curve.

Figure 4.10 shows the resolution limit as a function of the maximum half angle of a spherical cap. The angle observed ranges from around 0.8 radians to π radians (full sphere aperture). From the figure we see a decrease in the resolution limit, up to a certain point, where the resolution limit increases a bit before flattening out.

Lastly for the lens-less system, Figure 4.11 shows the resolution as a function of wavelength. This plot is the only thus far to have resolution as a function of meters. This is done to highlight the direct proportionality between the resolution limit and the wavelength.

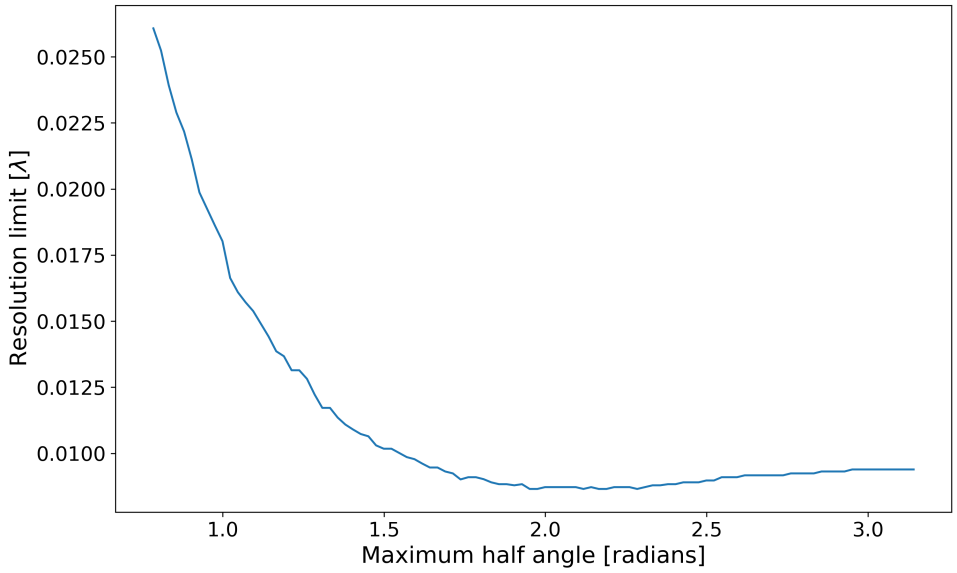

Figure 4.10: Resolution limit in wavelengths with respect to maximum half angle of aperture using MUSIC. The blue line represents a detector array in a spherical cap, covering an area corresponding to a numerical aperture = 1.2. The orange line represents a full spherical detector array.

Most of the results show a decrease in resolution limit when the effective aperture increases. The effective aperture in this case means how much of the electric field is collected. For the lens-less microscope, the detectors are discrete, point-like sampling points. If the number of sampling points increase, like in Figure 4.7, the electric field is sampled at more points, giving a better foundation for the reconstruction algorithm.

In Figure 4.8 the resolution limit increases with the radius of the imaging system. When the radius increases, the area of the aperture also increases. This gives a sparser sampling grid, and the effective aperture will decrease.

In Figure 4.10 the half angle of the imaging system is increased. The resolution limit first decreases with the half angle, but then increases a bit before flattening out. When the half angle increases, more regions of the sphere around the dipoles are sampled. This increase in area means more of the electric field will be made use of. The later increase in resolution limit may be a result of the sampling area increasing while the number of sampling points remain constant, resulting in sparser sampling. This sparser

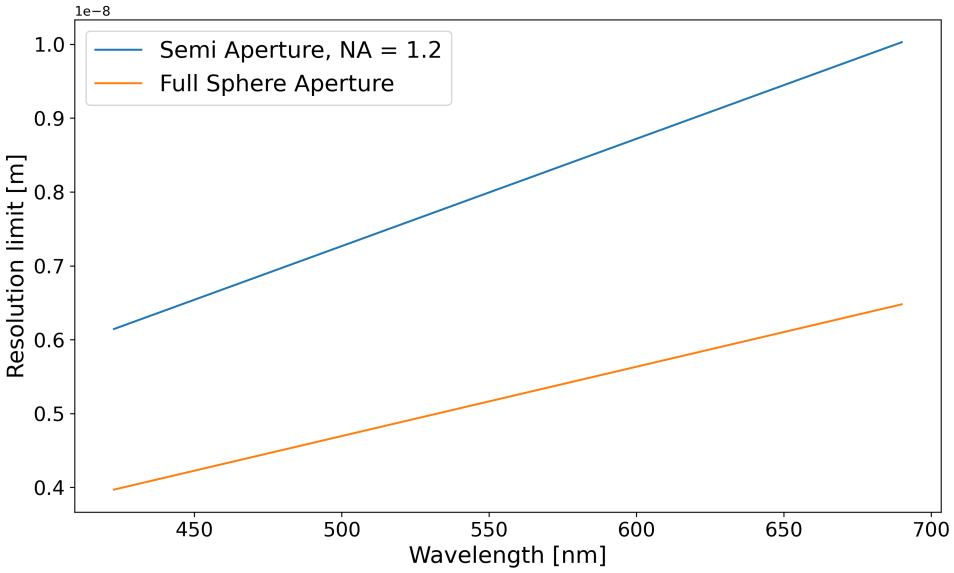

Figure 4.11: Resolution limit in wavelengths with respect to wavelength using MUSIC. The blue line represents a detector array in a spherical cap, covering an area corresponding to a numerical aperture = 1.2. The orange line represents a full spherical detector array.

sampling will then contribute more significant effects on the resolution than the increase in spherical coverage.

The commonality between all these variables is their contribution on the effective aperture. An increase in effective aperture will lead to a decrease of the resolution limit. This is the same effect the numerical aperture of a lens has in conventional microscopy. The other factors explored for this system is the number of time points, and wavelength.

For the number of time points, our polarization matrix will increase in size. This will allow the matrix to contain a wider variety of orientations. This again, will lead to a more diverse sampling of the DGF. This leads to a better reconstruction using the MUSIC algorithm. Although, increasing the number of samples beyond a certain point will give diminishing returns on the resolution limit.

When using MUSIC for reconstruction, the resolution limit is (for the standard variable values given in this paper) in the order of 10^{-2} wavelengths. Depending on the values we choose for the variables this can change

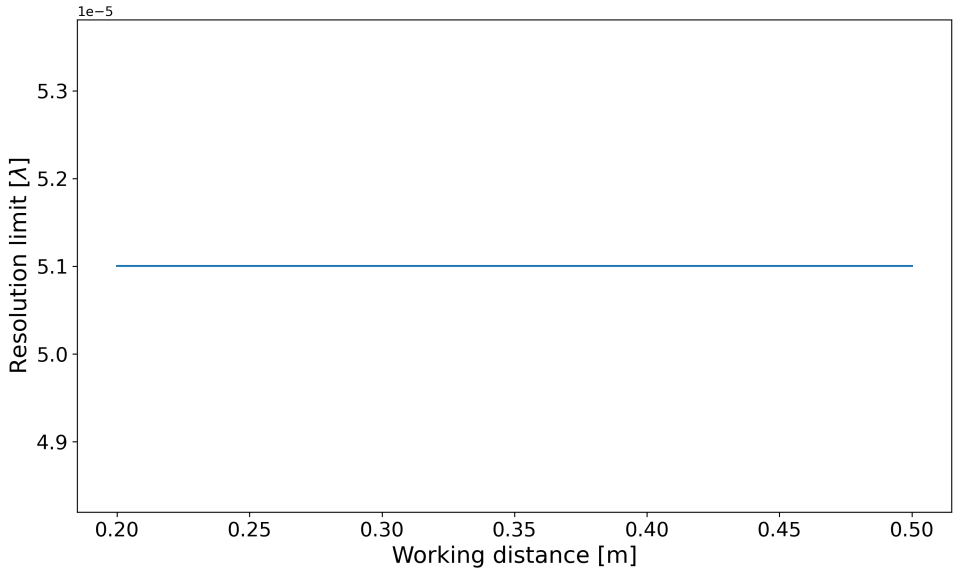

Figure 4.12: Resolution limit in wavelengths with respect to working distance. The system is a lens-based microscope using MUSIC for reconstruction.

significantly. If we compare this with the resolution using time reversal, we have an order of magnitude increase in resolution limit. The resolution using time reversal is calculated for a detector sphere radius of 10 wavelengths. Given this radius, the resolution using MUSIC would be significantly better.

Although MUSIC have a significantly better resolution than time reversal, MUSIC is a complex algorithm, while time reversal is less complex. Time reversal might be used for real time imaging, where resolution is not the main focus, while MUSIC can be used where better resolution is required.

4.2.2 Microscope

Applying MUSIC in conjunction to a microscope, as opposed to the lensless system, some of the variables of interest changes. One quick example of this can be seen in Figure 4.12, where the resolution limit of the system is given with respect to working distance (focal length) of the objective lens. Because the NA and magnification of the system is held constant, the working distance has no impact on the resolution. Another variable

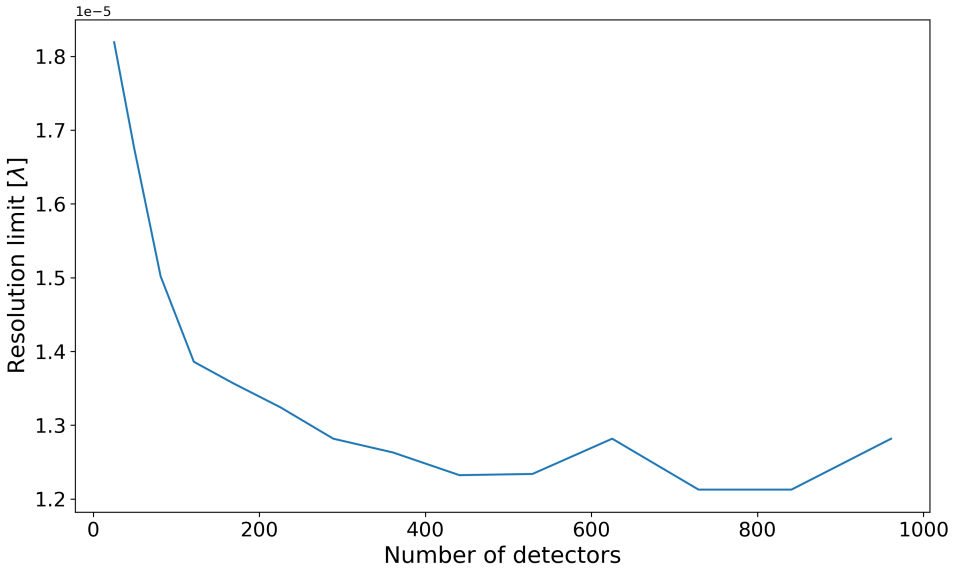

Figure 4.13: Resolution limit in wavelengths with respect to the number of detectors in camera array. The imaging system is a conventional microscope, using a square imaging array in the focus of the tube lens. using MUSIC for reconstruction.

needing change is the density of the imaging array. In the lens-less system, the density of the camera array was decided by the maximum half angle and the number of detectors. In this system, the detectors are distributed like a sensor array on the focal plane of the tube lens. Because of this, a new variable is introduces, called voxel size. As the detectors are simulated as point-like pixels, the voxel size will determine the distance between two detectors.

Like the simulations for the lens-less system, the only system variable changed is the one explored in a plot. The rest of the system is held constant, both for the simulation in question and the rest of the exploration of the other variables. The standard configurations for the system are as follows: number of detectors is held at 100, number of time points is held at 100, the numerical aperture of the objective lens is 1.2, wavelength is held at 690 nanometers, voxel size is kept at 3.6 microns, the magnification is held at 60×, and the immersion medium has a refractive index of 1.33.

Looking at Figure 4.13 the resolution limit is found with respect to the

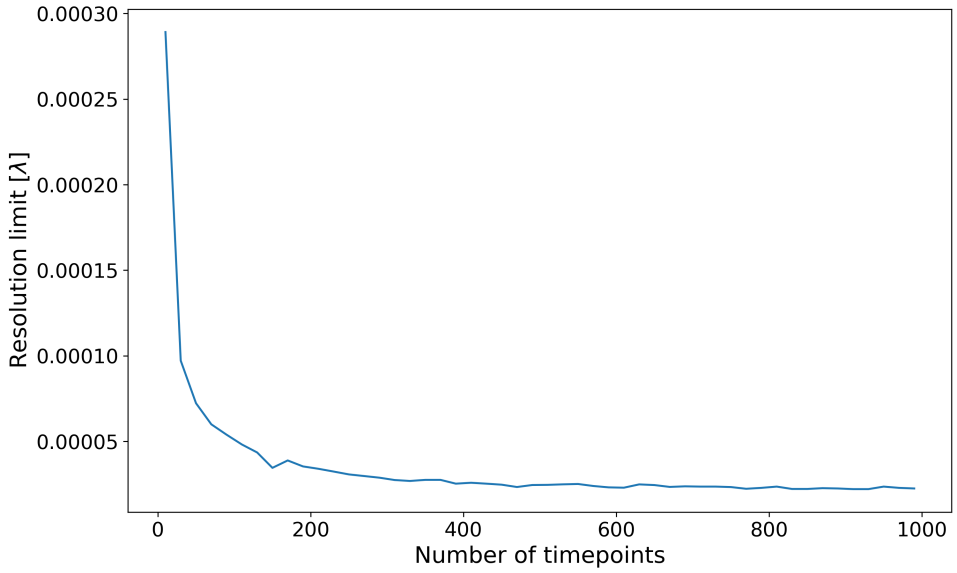

Figure 4.14: Resolution limit in wavelengths with respect to the number of time points imaged. The imaging system is a conventional microscope, using MUSIC for reconstruction.

number of sensors. This simulation has the lowest amount of reconstruction points. This is because the detectors are set in a square imaging array, allowing only square numbers of detectors to be reconstructed. The results, much like for the lens-less system, shows an inverse proportionality between the resolution limit and the number of sensors. There are two places where the resolution limit increases slightly, at 625 and 961 sensors. These increases in the resolution limit might be due to the placement of the detectors in the imaging array. As the number of detectors changes, the placement of each detector also changes to make the camera array centered in the system. This might move detectors from points on the PSF more suitable for reconstruction. This in turn might lead to a decrease in resolution limit.

Figure 4.14 shows the resolution limit with respect to the number of time points. The resolution limit is shown to decrease rapidly, and flatten out as the number of time points increases. This, as for the lens-less system, contributes to the variation of the electric field composing the covariance matrix used in MUSIC. The flattening out of the curve may be explained as diminishing return when as the polarization matrix grows.

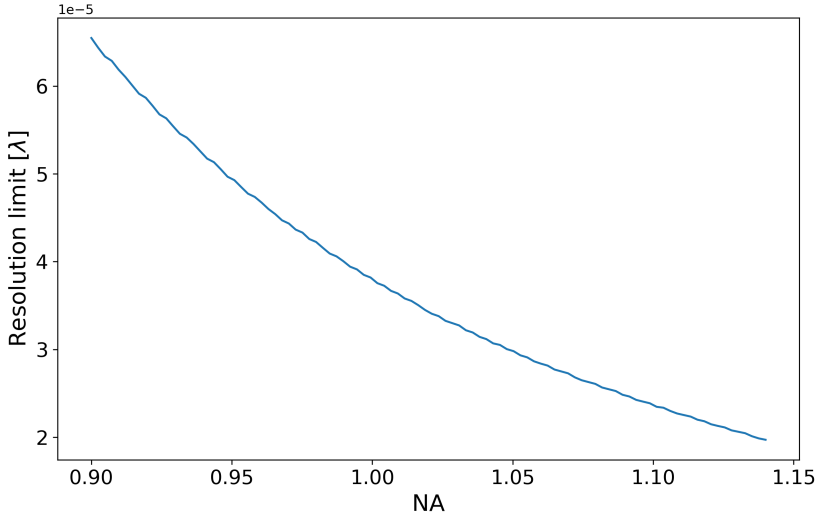

Figure 4.15: Resolution limit in wavelengths with respect to the numerical aperture. The imaging system is a conventional microscope, using MUSIC for reconstruction. The refractive index in the object space is constant and set to 1.33.

Next, Figure 4.15 shows the resolution limits with respect to numerical aperture. The shows the resolution limit to be inverse proportional to the numerical aperture. This is a direct analog to a conventional system, which is inverse proportional to the NA. This can be explained by the amount of the electric field being refracted by the objective lens.

Figure 4.16 and Figure 4.17 both show the resolution limit with respect to the voxel size. In Figure 4.16 the resolution limit is shown, while Figure 4.17 shows the base 10 logarithm of the resolution limit. This logarithm is to get a better sense of the order of magnitude of the resolution limit. From these plots, we can see the increase in the resolution limit as the voxel size increases. This indicates that a denser sampling will result in a better reconstruction. There are deviations to this increase where the resolution limit decreases in the middle of the graph. This might be explained the same way as with the increasing number of detectors, where the change in detector location results in the PSF being sampled at points not as viable for reconstruction.

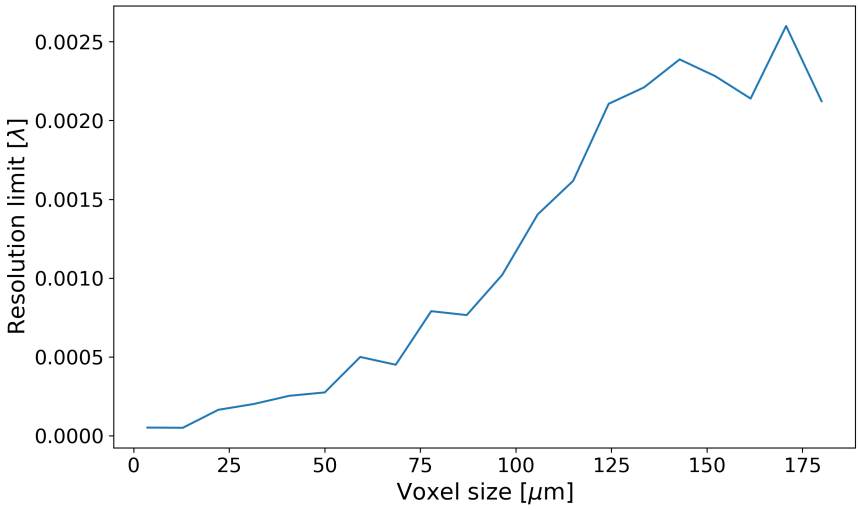

Figure 4.16: Resolution limit in wavelengths with respect to the voxel size of the camera array. The imaging system is a conventional microscope, using a square imaging array in the focus of the tube lens. using MUSIC for reconstruction. The pixels are point-like detectors, with the voxel size determining the distance between detectors.

Lastly, Figure 4.18 shows the resolution limit with respect to wavelength. The figure shows the resolution limit both in wavelengths and meters. From the plot we see a clear direct proportionality between the wavelength and the resolution limit. This means that the resolution limit will be proportional to the wavelength squared, as shown by the blue line in the figure. This is interesting, as for conventional microscopy, and for MUSIC for the lens-less system, the resolution limit is directly proportional to the wavelength.

As the reconstruction in this section uses a microscope to propagate the electric fields, we can compare this with conventional microscope resolutions for the same system. But the comparison between MUSIC and conventional microscopy is a bad one. An image using conventional microscopy can be found by a single time point, and using no reconstruction algorithm. Conversely, MUSIC uses several time points and a complex reconstruction algorithm to image make a single image.

Additionally, the results from the lens-less system and the lens-based

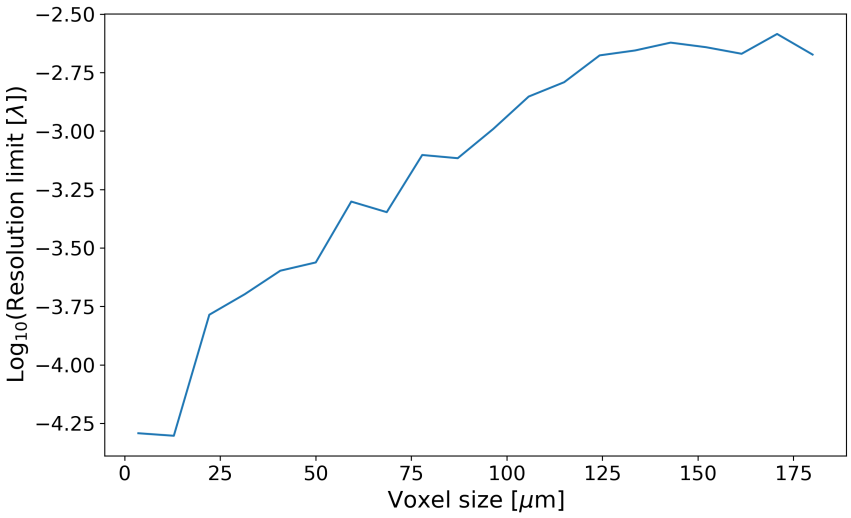

Figure 4.17: Base 10 logarithm of resolution limit in wavelengths with respect to the voxel size of the camera array. The imaging system is a conventional microscope, using a square imaging array in the focus of the tube lens. using MUSIC for reconstruction. The pixels are point-like detectors, wit the voxel size determining the distance between detectors.

system are compared. From the results we see a clear dependence on effective aperture from both systems. Though, for the lens-less system, this dependence is only linked to the detector density and maximum half angle. For the results, we also see orders of magnitude higher resolution for the lens-based system. This of course, only holds true close to the standard values chosen in this thesis. This increase in resolution for the lens-base system is possibly a result of the diffraction of the lenses. The light hitting the detectors at the camera is a superposition of all the light hitting the objective lens. This will increase the information we get from each pixel, and lay a better foundation for reconstruction of the dipole locations. This will give the lens-based system greater resolution, but this is not always needed. The increased cost of adding a microscope to the imaging array gives the lens-based system a disadvantage in some scenarios. For a lower cost system, where a resolution limit under 50 nm is not required, the lens-less system will be more desirable.

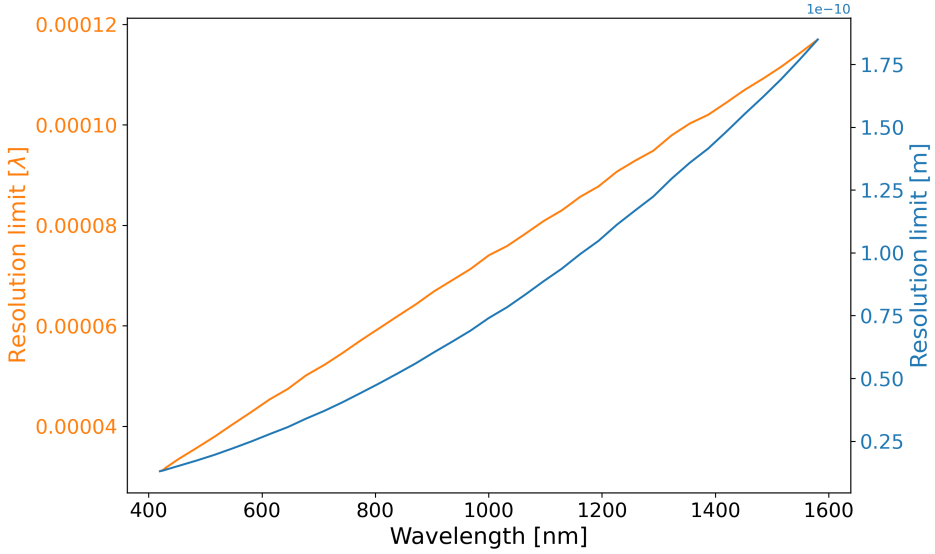

Figure 4.18: Resolution limit with respect to wavelength. The orange line shows the resolution limit with wavelength as the unit, while the blue line show the resolution limit in meters. The imaging system is a conventional microscope, using MUSIC for reconstruction.

CHAPTER 5

Exploratory Work For Intensity-Only Data and Further Studies

Image reconstruction using full electric fields results in great resolution, but the full electric field is often not available. The detectors suitable for use with wavelengths relevant to microscopy generally do not preserve phase information. This results in the detectors only giving intensity data. Using this intensity-only data to reconstruct images would be a valuable tool for a lens-less label-free system.

There are several techniques that might be used for intensity-only reconstructions. For this thesis, two possible techniques were explored, but eventually failed to provide adequate results. This might be due to the system design used, the applied cases being incompatible with the technique, or lack of deep understanding of the technique. The techniques covered here will be phase reconstruction and a modified MUSIC algorithm designed for intensity-only data.

5.1 Phase Reconstruction

Phase reconstruction is a method used for determining the full electric field based on intensity-only measurements. Using the resulting full electric field, methods for electric field reconstruction can be utilized. Two different methods can be found in [15], where they are called phaselift and quadratic inversion.

The intensity of an electric field is found by taking the square of the

absolute value of the electric field ($I = |E|^2$). This inherent non-linearity of intensity only data can make phase reconstruction difficult. Phaselift aims to circumvent this non-linearity by transforming it into a linear problem, and using a minimization algorithm to solve the linear problem. Quadratic inversion is based on inversion of the quadratic operator, and using gradient decent to find the electric field.

Though these techniques use different methods for finding the electric field, both rely on some knowledge of the electric field. In the paper exploring phaselift and quadratic inversion, the source of the electric field is assumed to be a monochromatic electric current in a cylinder. This allows for some knowledge of the shape of the emitted electric field. For the purposes of this thesis though, this a priori knowledge of the electric field was not available. The electric field scattered from an arbitrary amount of dipoles might be found, but was not done here. This lead to phase reconstruction being dismissed for the scope of this thesis.

5.2 Intensity-only MUSIC for lens-less system

One imaging technique using intensity-only data is subspace-based imaging[16, 17]. One of these methods use a modified MUSIC algorithm, relying on intensity-only data diversity to image small scatterers. In this section, a brief look at the modified algorithm will be presented, and some results will follow. For further reading, the algorithm is explored in detail in [16].

The main idea behind this algorithm comes from the identities:

$$|z_1 + z_2|^2 = |z_1|^2 + |z_2|^2 + 2\,\mathrm{Re}\left[z_1^* z_2\right], \tag{5.1}$$

$$|z_1 + iz_2|^2 = |z_1|^2 + |z_2|^2 - 2\,\mathrm{Im}\left[z_1^* z_2\right], \tag{5.2}$$

where z_1 and z_2 are arbitrary complex numbers. Combining these equations, we get:

$$\begin{aligned} z_1^* z_2 =& \frac{1}{2}\left[|z_1 + z_2|^2 - |z_1|^2 - |z_2|^2\right] \\ & - \frac{\mathrm{i}}{2}\left[|z_1 + \mathrm{i}z_2|^2 - |z_1|^2 - |z_2|^2\right] \end{aligned} \tag{5.3}$$

This identity can then be used to build a data matrix. By replacing z_1 and z_2 with electric fields originating from two light sources, and scattered by the dipoles. We can then reconstruct the product of these electric fields by only measuring intensity. We can then use different combinations of

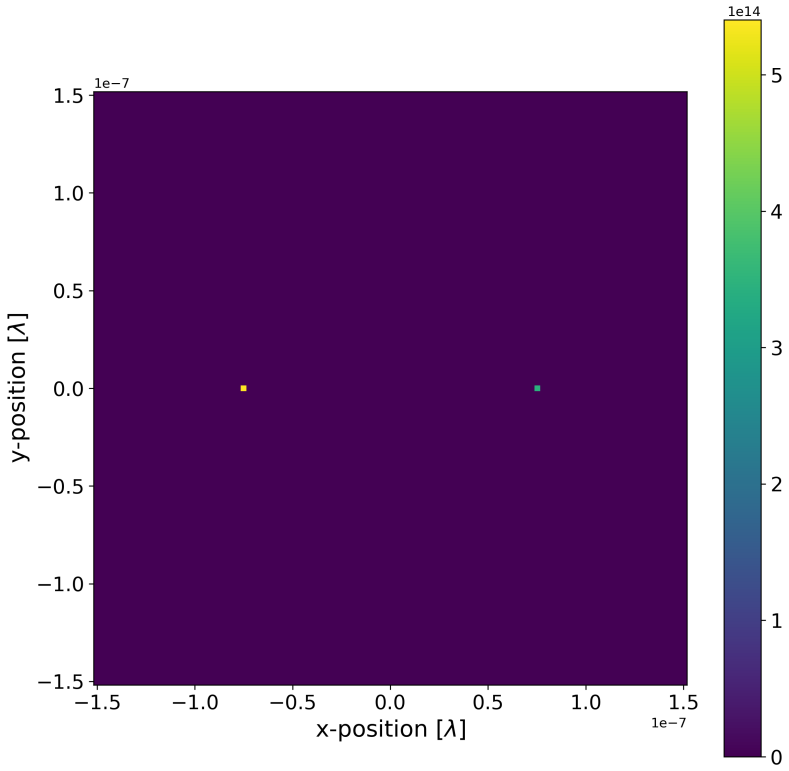

Figure 5.1: Intensity-only MUSIC reconstruction of a plane containing two resolved dipoles for noise-free data. The dipoles are separated by 152 nm, with a sampling grid containing the precise location of the dipole. The imaged wavelength was 690 nm, and the detector array had a radius of 0.016 m.

sources to make a better foundation for the reconstruction. The data vector will then look like:

$$\vec{\mathrm{x}} = (E_1^* E_1, E_1^* E_2, ..., E_1^* E_M), \tag{5.4}$$

where M is the number of light sources. This vector can be made for every

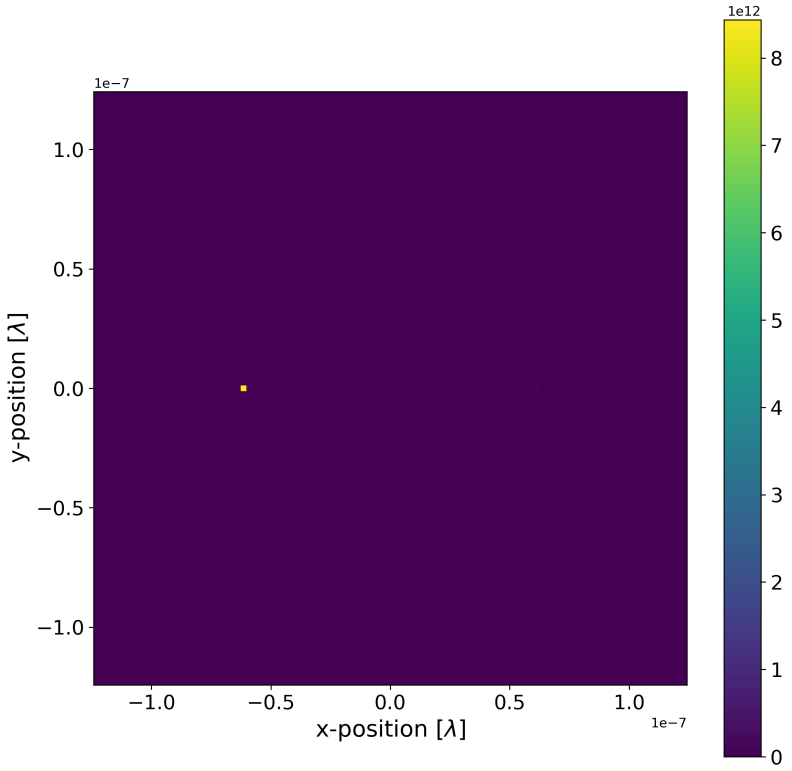

Figure 5.2: Intensity-only MUSIC reconstruction of a plane containing two dipoles for noise-free data. The dipoles are separated by 124 nm, with a sampling grid containing the precise location of the dipole. The imaged wavelength was 690 nm, and the detector array had a radius of 0.016 m. The reconstruction only shows one of the two dipoles present in the reconstruction, with the other dipole having a reconstruction estimate orders of magnitude less.

detector in the imaging array, and form a matrix $\mathbf{X}$ containing each data vector.

We then know the scattered light is decided by the DGF of the dipole,

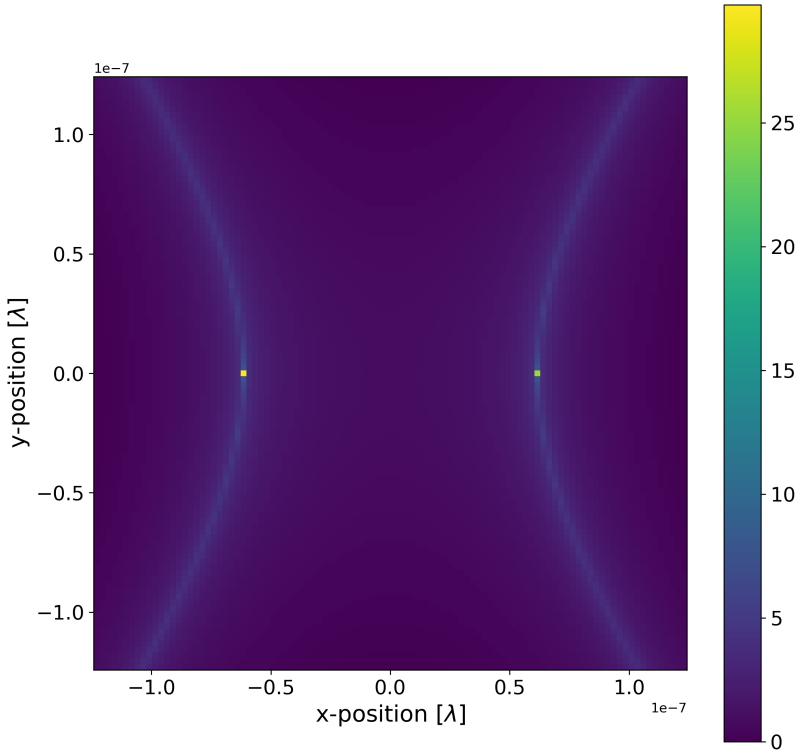

Figure 5.3: Base-e logarithm of intensity-only MUSIC reconstruction of a plane containing two dipoles for noise-free data. The dipoles are separated by 124 nm, with a sampling grid containing the precise location of the dipole. The imaged wavelength was 690 nm, and the detector array had a radius of 0.016 m.

scaled by the incoming light at the dipole location. Because only the light hitting the dipoles will contribute to the final field, the incoming light at the dipole locations will be a part of the data. This is then used for the reconstruction, assuming the data is a superposition containing the incident light at the dipole locations. The data matrix, $\mathbf{X}$, is then used in a singular

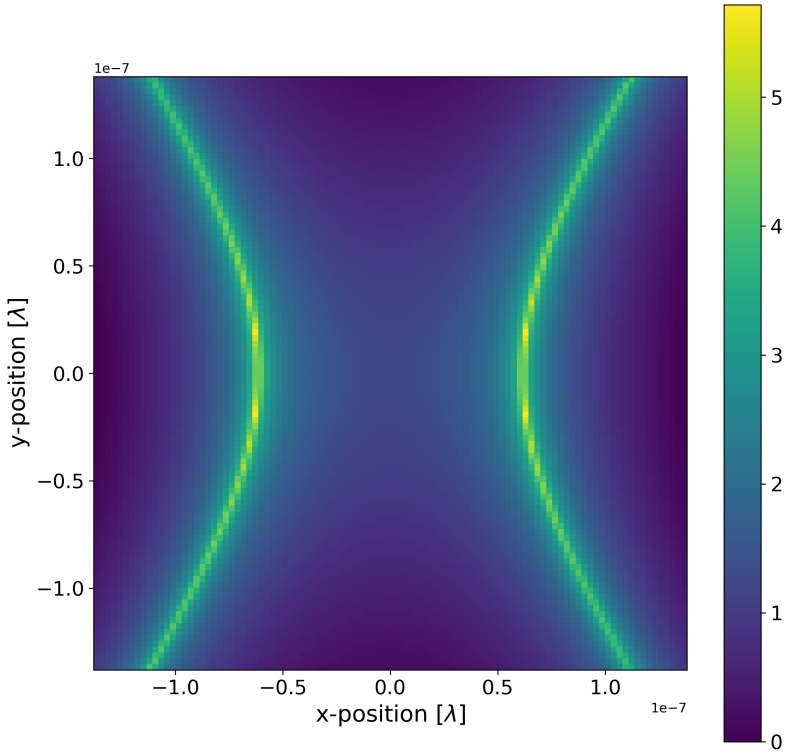

Figure 5.4: Base-e logarithm of intensity-only MUSIC reconstruction of a plane containing two dipoles for noise-free data. The dipoles are separated by 124 nm, with a sampling grid not containing the precise location of the dipole. The imaged wavelength was 690 nm, and the detector array had a radius of 0.016 m.

value decomposition. We then use the matrix composed of the inner product over all sensors, giving us information of the source pairs. The singular vectors are then separated into signal and noise by thresholding the singular values. The signal vectors are then used in the reconstruction, along with the incident waves at locations samples from the field of view.

This reconstruction algorithm may result in some good reconstruction. Figure 5.1 shows a reconstruction of two dipoles, set 0.22 wavelengths apart. The reconstruction was done using 100 light sources, 25 detectors, 690 nm wavelength, and a detector and source radius of 1.6 cm. The reconstruction has two clearly resolved points.

The distance between the dipoles was then changed to 0.18 wavelengths, and the same setup was used to reconstruct the dipoles. This reconstruction is shown in Figure 5.2 and we can observe only one dipole, but the second is present. The natural logarithm of this reconstruction can be found in Figure 5.3. Here we see the two dipoles are both present in the reconstruction. There are also two lines in the reconstruction. The incident fields at these locations are also contained in the data. This shows a clear weakness of the reconstruction. To get a clearer picture of this, the dipoles are given a little offset in the x-direction (the direction the dipoles are separated in), while the distance is kept the same. This reconstruction is seen in Figure 5.4, and is set in the log scale. In this reconstruction we see no dipoles, but two lines. If we then move the sampling grid equal to the dipoles, the result is the same as in Figure 5.3. This shows the reconstruction algorithm to be way too sensitive to the sampling grid, giving ambiguous answers when not sampling the exact position of the dipole.

The sensitivity of the sampling grid, giving ambiguous answers when not sampling the exact dipole location, makes the technique less than ideal for most use cases. Though with more time and effort, the method might be useful. One possibility with the technique is to make one reconstruction, and then sample finer along the reconstruction lines. The use of the algorithm with more than two dipoles are not explored though, and might give different types of results than the ones given here. The technique is ultimately worth further studies.

5.3 MUSIC for microscope

In the MUSIC reconstruction for a microscope system, the resolution seems to be proportional to the wavelength squared. This result was ultimately the most interesting result of this theses, and is worth further studies. An attempt was done, calculating the resolution limit for the same variables, using noisy data. Though, due to time restriction this was not explored in this thesis.

CHAPTER 6

Conclusion

This thesis have investigated the feasibility of label-free microscopy using full electric field analysis, and compared a lens-less system with a conventional lens-based microscope. The systems shows similarity in their dependence of effective aperture size, but showing the lens-based system to have orders of magnitude better resolution limit.

The main difference in the results was the proportionality between the resolution limit and the wavelength. While the lens-less system was linearly-proportional to the wavelength, the lens-based system had a non-linearly proportionality with the wavelength. The non-linearity of the resolution limit likely stem from the wavelength dependence in the microscope DGF. This non-linear dependence on wavelength introduces a new research path for future work.

The reconstructions using a lens-based system gives higher resolution, probably caused by the numerical aperture of the objective lens being higher than the effective aperture of a point-like sampling grid. Though, this increase in resolution comes at the cost of a more expensive system, requiring a setup containing a conventional microscope. The lens-based system also suffers from higher reconstruction time, and increased simulation and system complexity. This makes the two systems a viable option in different cases.

The feasibility of a lens-less system using intensity-only reconstruction was also considered. While giving good preliminary results, the method was discarded due to ambiguity in the reconstruction, originating from a sensitivity of the sampling grid. While being discarded in this thesis, the method achieved super-resolution under specific circumstances. The use of intensity-only reconstruction to achieve super-resolution is a topic for future

work.

Appendices

APPENDIX A

Implementation

All data collection, image reconstruction, and image processing was done using the Python programming language. A full list of the essentials used, as well as their use in the code, are given in Appendix B.

The simulation implementation used for this thesis can be found at `https://github.com/JonSommernes/Master-Fishbowl-`. Due to time limitations, the quality and readability of the code may vary significantly.

APPENDIX B

Python Packages

This section gives a list of the most essential packages used for the imaging simulation, as well as their use in the implementation.

B.1 Numpy

Numpy is a powerful tool for numerical computation, especially for matrix operations[18]. The numpy package is an open source, and mostly written in well optimized C code.

For the simulations in this thesis, numpy was widely used for many mathematical operations, and most matrix operations.

B.2 Scipy

Scipy is a scientific computing package for python[19]. The package contains many commonly used functions, like integration in up to n dimensions, Fourier transforms, and Bessel functions.

For this thesis, scipy was mostly used for integration, and Bessel functions.

B.3 Numba

Numba is a package made for just-in-time compilation of python[20]. The package translates python and numpy code into fast machine code to speed execution of code. The package has no need for any external compiler, and can accelerate functions using multi-threading and GPU.

In this project, numba was widely used to accelerate functions to speed up simulation time. This cut some simulation batches down from days, to hours, to run.

B.4 Pillow

Pillow is a library widely used for image processing[21]. The package has many functions widely used in image processing, and functions for easily saving and reading image files.

For this project, Pillow was only used for saving and reading image files, using the tiff format.

B.5 Matplotlib

Matplotlib is a library for creating visualizations in python[22]. The package can be used to create plots, images, or animations using data from python or numpy arrays.

In this thesis, matplotlib was widely used for image reconstruction and analysis.

APPENDIX C

Algorithm implementations

C.1 Fibonacci mapping

The Fibonacci mapping is an algorithm for distributing points near-uniformly on a spherical surface. Following here will be the algorithm written in pseudo-code, with comments to understand the mapping algorithm.

Algorithm 1 Fibonacci mapping

procedure
    $N_{det} \leftarrow$ Number of detectors
    $radius \leftarrow$ Radius of the detector array
    $\phi = \pi * (3 - \sqrt{5}) \leftarrow$ Golden angle in radians
    $det\_loc \leftarrow$ Array of shape $N_{det} \times 3$ to hold detector location
    for i in range $(0, N_{det} - 1)$ **do**
        $y = 1 - \left(\frac{i}{N_{det}-1}\right) * 2 \leftarrow$ y ranges from 1 to -1
        $r = \sqrt{1 - y^2} \leftarrow$ Find the radius from the y-axis to the intersection between the sphere surface and the xz-plane
        $\theta = phi * i \leftarrow$ Using golden angle increment to find theta
        $x = \cos\theta * r \leftarrow$ Using theta and radius to determine x-position
        $z = \sin\theta * r$
        $det\_loc[i] = (x, y, z) \leftarrow$ Put the detector coordinates into the detector array
    $det\_loc = det\_loc * radius \leftarrow$ Scale the positions of the detectors with the sphere radius

C.2 Resolution limit

Algorithm 2 Resolution limit

```
1: procedure
2:     while run = True do
3:         dipoles ← Positions of dipole pair
4:         dist ← Distance between dipoles
5:         if dipoles = resolvable then
6:             dipole_1 = −dist/4 ← Halves the distance between the dipoles
7:             dipole_2 = dist/4
8:             tmp = dist ← Saves the current resolvable distance
9:         if dipoles = not resolvable then
10:            x_1 = dist/2 ← Position of current dipole
11:            x_2 = tmp/2 ← Position of resolved dipole
12:            x = (x_1+x_2)/2 ← New distance to dipole
13:            dipole_1 = −x ← Set new dipole position
14:            dipole_1 = x
15:        if (dist-tmp)/dist < 0.01 then
16:            run = False ← When distance from resolved dipole to
    current dipole is less than 1% of distance to dipole, the loop stops
```

Bibliography

[1] Matthew R Arnison and Colin JR Sheppard. "A 3D vectorial optical transfer function suitable for arbitrary pupil functions". In: *Optics communications* 211.1-6 (2002), pp. 53–63.

[2] Giuseppe Vicidomini. "Image Formation in Fluorescence Microscopy". In: *From Cells to Proteins: Imaging Nature across Dimensions*. Ed. by Valtere Evangelista et al. Dordrecht: Springer Netherlands, 2005, pp. 371–393. ISBN: 978-1-4020-3616-3.

[3] Aurélie Jost and Rainer Heintzmann. "Superresolution multidimensional imaging with structured illumination microscopy". In: *Annual Review of Materials Research* 43 (2013), pp. 261–282.

[4] Zicheng Liu and Krishna Agarwal. "Silicon substrate significantly alters dipole-dipole resolution in coherent microscope". In: *Optics Express* 28.26 (2020), pp. 39713–39726.

[5] Leung Tsang, Jin Au Kong, and Kung-Hau Ding. *Scattering of electromagnetic waves: theories and applications*. Vol. 27. John Wiley & Sons, 2004.

[6] Zicheng Liu and Krishna Agarwal. *Supplementary document for Silicon substrate significantly alters dipole-dipole resolution in coherent microscope - 4832318.pdf*. Dec. 2020. DOI: 10.6084/m9.figshare.13187783.v2. URL: https://osapublishing.figshare.com/articles/journal_contribution/Supplementary_document_for_Silicon_substrate_significantly_alters_dipole-dipole_resolution_in_coherent_microscope_-_4832318_pdf/13187783/2.

[7] Hossein M Manesh et al. "A new method to locate faults in power networks based on electromagnetic time reversal". In: *2012 IEEE 13th International Workshop on Signal Processing Advances in Wireless Communications (SPAWC)*. IEEE. 2012, pp. 469–474.

[8] Geoffroy Lerosey et al. "Focusing beyond the diffraction limit with far-field time reversal". In: *Science* 315.5815 (2007), pp. 1120–1122.

[9] GEOFFREY F Edelmann. "An overview of time-reversal acoustic communications". In: *Turkish International Conference in Acoustics*. 2005.

[10] Gabriel Montaldo et al. "The time reversal kaleidoscope: a new concept of smart transducers for 3d imaging". In: *IEEE Symposium on Ultrasonics, 2003.* Vol. 1. IEEE. 2003, pp. 42–45.

[11] AO Maksimov and Yu A Polovinka. "Time reversal technique for gas leakage detection". In: *The Journal of the Acoustical Society of America* 137.4 (2015), pp. 2168–2179.

[12] Qian Xu et al. "Security-aware waveform and artificial noise design for time-reversal-based transmission". In: *IEEE Transactions on Vehicular Technology* 67.6 (2018), pp. 5486–5490.

[13] Victor Barsan and Radu Lungu. *Trends in Electromagnetism: From Fundamentals to Applications*. BoD–Books on Demand, 2012.

[14] Ralph Schmidt. "Multiple emitter location and signal parameter estimation". In: *IEEE transactions on antennas and propagation* 34.3 (1986), pp. 276–280.

[15] Raffaele Moretta and Rocco Pierri. "Performance of phase retrieval via phaselift and quadratic inversion in circular scanning case". In: *IEEE Transactions on Antennas and Propagation* 67.12 (2019), pp. 7528–7537.

[16] Arnold D Kim and Chrysoula Tsogka. "Intensity-only inverse scattering with MUSIC". In: *JOSA A* 36.11 (2019), pp. 1829–1837.

[17] Li Pan et al. "Subspace-based optimization method for inverse scattering problems utilizing phaseless data". In: *IEEE Transactions on Geoscience and Remote Sensing* 49.3 (2010), pp. 981–987.

[18] Charles R. Harris et al. "Array programming with NumPy". In: *Nature* 585.7825 (Sept. 2020), pp. 357–362. DOI: 10.1038/s41586-020-2649-2. URL: https://doi.org/10.1038/s41586-020-2649-2.

[19] Pauli Virtanen et al. "SciPy 1.0: Fundamental Algorithms for Scientific Computing in Python". In: *Nature Methods* 17 (2020), pp. 261–272. DOI: 10.1038/s41592-019-0686-2.

[20] Siu Kwan Lam, Antoine Pitrou, and Stanley Seibert. "Numba: A llvm-based python jit compiler". In: *Proceedings of the Second Workshop on the LLVM Compiler Infrastructure in HPC*. 2015, pp. 1–6.

[21] Alex Clark. *Pillow (PIL Fork) Documentation*. 2015. URL: https://buildmedia.readthedocs.org/media/pdf/pillow/latest/pillow.pdf.

[22] J. D. Hunter. "Matplotlib: A 2D graphics environment". In: *Computing in Science & Engineering* 9.3 (2007), pp. 90–95. DOI: 10.1109/MCSE.2007.55.